POLITECNICO DI TORINO
Repository ISTITUZIONALE

Impact of nickel–titanium super-elastic material properties on the mechanical performance of self-expandable transcatheter aortic valves

Original
Impact of nickel–titanium super-elastic material properties on the mechanical performance of self-expandable transcatheter aortic valves / Carbonaro, D., Zambon, S., Corti, A., Gallo, D., Morbiducci, U., Audenino, A.L., Chiastra, C.. - In: JOURNAL OF THE MECHANICAL BEHAVIOR OF BIOMEDICAL MATERIALS. - ISSN 1751-6161. - ELETTRONICO. - 138:(2023), p. 105623. [10.1016/j.jmbbm.2022.105623]

Availability:
This version is available at: 11583/2974796 since: 2023-01-19T10:31:59Z

Publisher:
Elsevier BV

Published
DOI:10.1016/j.jmbbm.2022.105623

Terms of use:

This article is made available under terms and conditions as specified in the corresponding bibliographic description in the repository

Publisher copyright

(Article begins on next page)

26 November 2026

Accepted manuscript at https://linkinghub.elsevier.com/retrieve/pii/S1751-6161(22)00528-8

Impact of Nickel-Titanium super-elastic material properties on the mechanical performance of self-expandable transcatheter aortic valves

Dario Carbonaro[1], Sara Zambon[1], Anna Corti[2], Diego Gallo[1], Umberto Morbiducci[1], Alberto Audenino[1], Claudio Chiastra[1*]

1. PoliTo[BIO]Med Lab, Department of Mechanical and Aerospace Engineering, Politecnico di Torino, Turin, Italy
2. LaBS, Department of Chemistry, Materials and Chemical Engineering "Giulio Natta", Politecnico di Milano, Milan, Italy

***Address for correspondence:**

Claudio Chiastra, PhD

PoliTo[BIO]Med Lab

Department of Mechanical and Aerospace Engineering

Politecnico di Torino

Corso Duca degli Abruzzi, 24

10129 Turin, Italy

ORCID: 0000-0003-2070-6142

E-mail: claudio.chiastra@polito.it

Post-print

Accepted manuscript at https://linkinghub.elsevier.com/retrieve/pii/S1751-6161(22)00528-8

Abstract

Self-expandable transcatheter aortic valves (TAVs) elastically resume their initial shape when implanted without the need for balloon inflation by virtue of the Nickel-Titanium (NiTi) frame super-elastic properties. Experimental findings suggest that NiTi mechanical properties can vary markedly because of a strong dependence on the chemical composition and processing operations. In this context, this study presents a computational framework to investigate the impact of the NiTi super-elastic material properties on the TAV mechanical performance. Finite element (FE) analyses of TAV implantation were performed considering two different TAV frames and three idealized aortic root anatomies, evaluating the device mechanical response in terms of pullout force magnitude exerted by the TAV frame and peak maximum principal stress within the aortic root. The widely adopted NiTi constitute model by Auricchio and Taylor (1997) was used. A multi-parametric sensitivity analysis and a multi-objective optimization of the TAV mechanical performance were conducted in relation to the parameters of the NiTi constitutive model. The results highlighted that: five NiTi material model parameters (E_A, σ_{tL}^S, σ_{tU}^S, σ_{tU}^E and σ_{cL}^S) are significantly correlated with the FE outputs; the TAV frame geometry and aortic root anatomy have a marginal effect on the level of influence of each NiTi material parameter; NiTi alloy candidates with pareto-optimal characteristics in terms of TAV mechanical performance can be successfully identified. In conclusion, the proposed computational framework supports the TAV design phase, providing information on the relationship between the super-elastic behavior of the supplied NiTi alloys and the device mechanical response.

Keywords: transcatheter aortic valve implantation, self-expanding device, Nitinol, finite element analysis, surrogate modelling, sensitivity analysis, optimization.

Post-print

Accepted manuscript at https://linkinghub.elsevier.com/retrieve/pii/S1751-6161(22)00528-8

1. Introduction

Transcatheter aortic valve (TAV) implantation has become a widely adopted alternative to open heart surgical valve replacement for the treatment of severe aortic stenosis in intermediate - to high-risk patients (Tabata et al., 2019). The advantages provided by the minimally invasive approach (Marquis-Gravel et al., 2016) and the clinical effectiveness in intermediate-risk patients (Cubero-Gallego et al., 2020; Howard et al., 2019) have recently suggested to extend the use of TAVs also to low-risk patients (Mack et al., 2019; Popma et al., 2019). Currently, technological improvements are under analysis to overcome the complications still affecting TAV implantation (Rotman et al., 2018), such as paravalvular regurgitation, conduction abnormalities and vascular complications (Howard et al., 2019), in order to improve their safety and effectiveness (Tiyerili et al., 2022).

TAVs are commonly composed of a bioprosthetic valve sutured on a metal frame (Fanning et al., 2013) and can be grouped into balloon-expandable and self-expandable valves, featured by a cobalt-chromium, stainless steel or a nickel-titanium (NiTi) frame, respectively (Jones et al., 2017). Differently from the balloon-expandable TAVs, which are plastically deformed when released from the catheter and expanded through balloon inflation into the aortic root, self-expandable TAVs elastically resume their initial shape within the implantation site, after being subjected to high strains when crimped into the delivery system (Dasi et al., 2017). Indeed, NiTi has established itself as the material of election for the frame of self-expandable TAVs, owing to its super-elastic material property, which can be operatively translated into the ability to elastically sustain high strain values at body temperature (Stoeckel et al., 2004). This unique property is associated with the transformation between two solid phases in the NiTi lattice structure, referred to as austenite, which is stable at low strain values and at body temperature, and martensite, which is stable at high strain values (Otsuka and Ren, 2005). The typical NiTi uniaxial stress *vs.* strain curve (Fig. 1) is characterized by an elastic hysteresis, with two

Post-print

plateaus in the loading and unloading phases, where high strains are generated and recovered, respectively. This material property has a remarkable impact on the TAV mechanical performance and on its clinical effectiveness as well (Finotello et al., 2021), and needs to be carefully accounted for during the design phase of the device.

From a biomechanical viewpoint, the design of TAVs is a challenging task as it involves the fulfillment of multiple requirements, including the exertion of a sufficiently high pullout force to prevent valve migration (McGee et al., 2019b; Mummert et al., 2013), and simultaneously the generation of low stresses within the aortic root to limit the risk of tissue tearing (Wang et al., 2015). Within this context, finite element (FE) modelling is an effective tool for supporting TAV design, with great benefits in terms of device optimization (Barati et al., 2021, 2022; Carbonaro et al., 2021; Rocatello et al., 2019a) and reduction of times and costs associated with the iterative prototyping phase and related experimental tests (Cabrera et al., 2017; Petrini et al., 2017b).

To date, several computational studies have been performed to investigate the mechanical behavior of self-expandable TAVs (an overview of the literature is presented in Table 1). In such studies, the NiTi super-elastic material properties of the TAV frame have been described through the constitutive model developed by Auricchio and Taylor (1997). Given a certain temperature, this constitutive model requires eight parameters to describe the NiTi material uniaxial tension and compression curve (Fig. 1), considering that the austenite and martensite Poisson ratios are usually set to 0.3 in literature (Berti et al., 2022). The NiTi material model parameters used in the computational studies reported in Table 1 and adopting the NiTi constitutive model of Fig. 1 proposed by Auricchio and Taylor (1997) are summarized in Table 2. In detail, eleven combinations of NiTi material model parameters (corresponding to eleven NiTi materials with different mechanical properties) emerged from the literature. The exploration of the literature also highlighted the use of different NiTi material model parameters applied to the study of the mechanical behavior of the same TAV design. In the

Post-print

absence of information on the material properties provided by the TAV manufacturers, different strategies were adopted to retrieve the values of NiTi material model parameters: Tzamtzis et al. (2013) (Material #1), Cabrera et al. (2017) (Materials #3-5), Carbonaro et al. (2020) (Material #7) and Finotello et al. (2021) (Materials #8-11) estimated the NiTi material model parameters through calibration with experimental tests directly conducted on TAVs (i.e., considering the entire devices); Petrini et al. (2017b) (Material #6) performed uniaxial tests on NiTi specimens. The other research groups listed in Table 1 referred to the previously cited works.

The range of variation of the NiTi material model parameters used in the computational studies on self-expandable TAVs as emerged from the literature survey is large (Table 2) and consistent with experimental findings, suggesting that the super-elastic material properties of NiTi are strongly influenced by the material chemical composition, grain size and distribution, and by the processing operations and history (Liu and Mishnaevsky, 2013; Mwangi et al., 2019; Valiev et al., 2020). The NiTi material microstructure and the associated mechanical properties are markedly sensitive to the Nickel / Titanium ratio in the alloy as well as to the time duration and operating temperatures of the applied heat treatments (Hodgson and Russell, 2000). Hence, the mechanical performance and clinical outcomes of TAVs could be severely affected by the different NiTi alloys their metal frame could be made of.

The present work lies in this context and aims to develop a computational framework to investigate the impact that the values of the parameters identifying the NiTi super-elastic constitutive model have on TAV mechanical performance. Technically, the computational framework combines FE analysis of TAV frame implantation and surrogate modelling to perform a sensitivity analysis exploring the relationship between the NiTi material model parameters and the TAV mechanical performance. The sensitivity analysis is conducted considering different TAV frame designs implanted in idealized aortic root models to elucidate to which extent the results of the sensitivity analysis depend

Post-print

on specific TAV frame geometries and aortic root anatomies. Furthermore, a multi-objective optimization of the TAV mechanical performance in relation to the NiTi material model parameters is included in the framework.

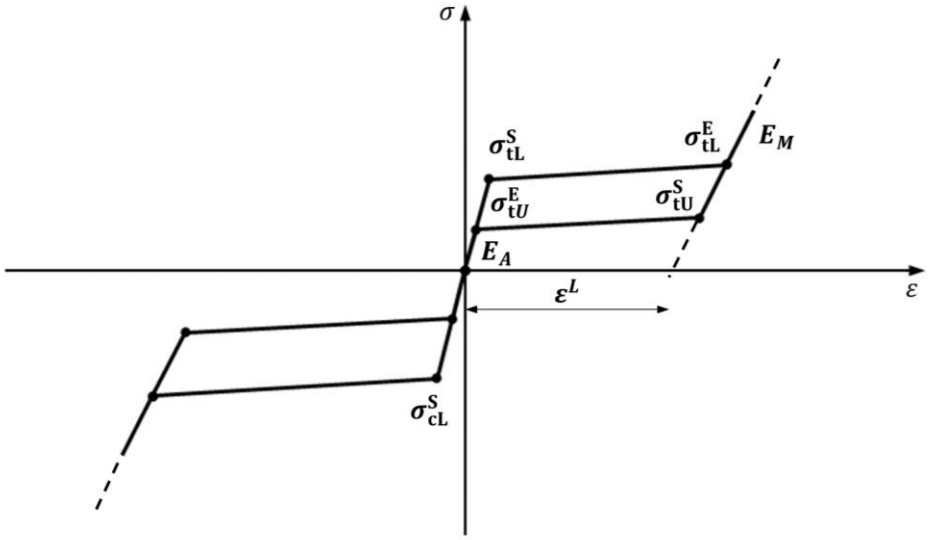


Fig. 1. Uniaxial tension and compression stress *vs.* strain curve of NiTi at 37 °C, with reference to the super-elastic material model parameters used in Abaqus: austenite elastic modulus E_A, martensite elastic modulus E_M, uniaxial transformation strain ε^L, starting stress of transformation in traction loading σ^S_{tL}, ending stress of transformation in traction loading σ^E_{tL}, starting stress of reverse transformation in traction unloading σ^S_{tU}, ending stress of reverse transformation in traction unloading σ^E_{tU}, starting stress of transformation in compression loading σ^S_{cL}. Accordingly, the description of the NiTi tensile behavior is based on seven parameters, while that of the compression behavior is simplified by using only the parameter σ^S_{cL}, scaling the tensile strain and stress quantities by the ratio of $\sigma^S_{cL}/\sigma^S_{tL}$.

Post-print

Table 1. List of publications on FE models of self-expandable TAVs. For each study the considered device and the associated number of the TAV frame NiTi material are indicated. Refer to Table 2 for retrieving the NiTi material model parameters associated with each material number.

First author and year	Manufacturer	TAV Device	Material number
(Tzamtzis et al., 2013)	Medtronic	CoreValve	1
(Gunning et al., 2014)	-	TAV prototype	1
(Ovcharenko et al., 2016)	Medtronic	Medtronic - CoreValve	1
(Bosi et al., 2015)	Medtronic	Medtronic - CoreValve	1
(Bosmans et al., 2016)	Medtronic	Medtronic - CoreValve	1
(Morganti et al., 2016)	Medtronic	Medtronic - CoreValve	2
(Cabrera et al., 2017)	pfm medical	TAV prototype	3/4/5
(Finotello et al., 2017)	Medtronic	CoreValve	2
(Petrini et al., 2017b)	-	TAV prototype	6
(Mao et al., 2018)	Medtronic	CoreValve	1
(Rocatello et al., 2019b)	Medtronic	CoreValve	2
(Bianchi et al., 2019)	Medtronic	CoreValve	2
(Carbonaro et al., 2020)	Aortic Lab	TAV with anti-embolic filter	7
(Ghosh et al., 2020)	Medtronic	CoreValve	2
(Luraghi et al., 2020)	Medtronic	CoreValve Evolut R	2
(Bosi et al., 2020)	Medtronic	CoreValve	1
(Kusneri et al., 2021)	Medtronic	CoreValve Evolut R	2
(Carbonaro et al., 2021)	Medtronic	CoreValve	2
(Finotello et al., 2021)	Boston Scientific	Acurate Neo	8
	Abbott	Portico	9
	Medtronic	Evolut	10
	Medtronic	CoreValve	11
(Pasta and Gandolfo, 2021)	Medtronic	Evolut	2

Medtronic (Dublin, Ireland); pfm medical (Cologne, Germany); Aortic Lab (Savigny, Switzerland); Boston scientific (Marlborough, MA, USA); Abbott (Abbott Park, IL, USA)

Post-print

Table 2. Super-elastic material model parameters associated to NiTi material numbers reported in Table 1. Refer to Fig. 1 for the visualization of the NiTi material parameters.

Material number	1	2	3	4	5	6	7	8	9	10	11
E_A (MPa)	50000	51700	58000	88000	78000	46900	45000	50000	55000	44000	51700
E_M (MPa)	25000	47800	22000	22000	22000	18358	19000	35000	40000	20000	50000
ε^L	0.07	0.063	0.0405	0.0405	0.0405	0.0496	0.0455	0.08	0.095	0.055	0.063
σ_{tL}^S (MPa)	380	600	480	300	350	305	330	510	500	460	730
σ_{tL}^E (MPa)	400	670	550	420	420	364	345	680	600	465	850
σ_{tU}^S (MPa)	250	288	320	150	150	182	240	430	380	360	440
σ_{tU}^E (MPa)	220	254	170	50	50	126	130	410	340	260	390
σ_{cL}^S (MPa)	NA	900	560	560	550	467.6	330	900	900	900	900

E_A: austenite elastic modulus, E_M: martensite elastic modulus, ε^L: uniaxial transformation strain, σ_{tL}^S: starting stress of transformation in traction loading, σ_{tL}^E: ending stress of transformation in traction loading, σ_{tU}^S: starting stress of reverse transformation in traction unloading, σ_{tU}^E: ending stress of reverse transformation in traction unloading, σ_{cL}^S: starting stress of transformation in compression loading, NA: not available.

2. Methods

The procedure used to study the impact of the NiTi material model parameter variability on the TAV mechanical performances consisted of the following main steps (Fig. 2): (1) FE modelling of the TAV implantation procedure, considering different deployment scenarios in terms of TAV design and idealized aortic root configuration, to obtain quantifications of the pullout force magnitude exerted by the TAV frame and the peak maximum principal stress within the aortic root; (2) coupling the design of experiment method with surrogate modelling to define an approximate relationship between FE outputs and NiTi material model parameters of the TAV frame in their possible range of variation; (3) multi- and mono-parametric sensitivity analysis of the material model parameters value *vs.* TAV mechanical performance; (4) parallel to point (3), identification of pareto-optimal NiTi material model parameters

Post-print

values assuring adequate TAV mechanical performance.

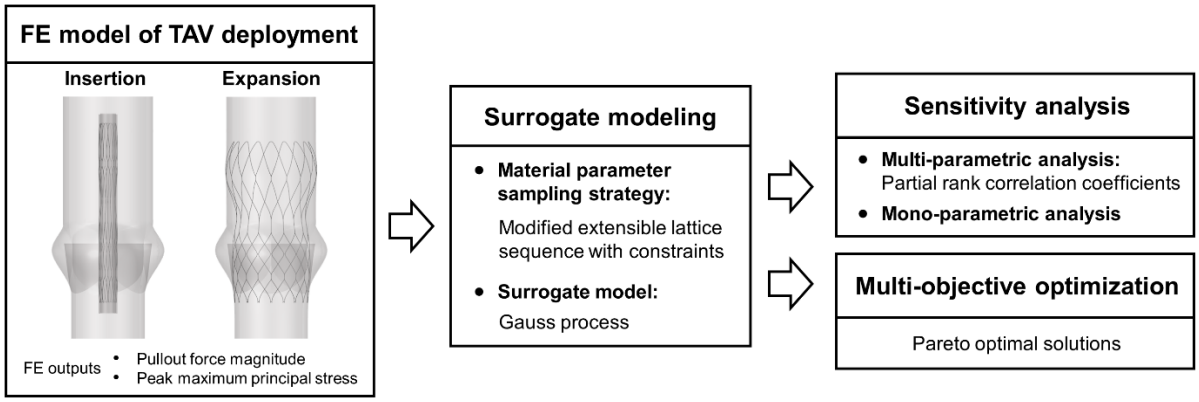


Fig. 2. Main steps of the computational framework: (1) FE modelling of TAV implantation procedure for the quantification of the pullout force exerted by the TAV frame and peak maximum principal stress within the aortic root; (2) NiTi material model parameters sampling and implementation of surrogate models of the two FE outputs; (3) multi- and mono-parametric sensitivity study of the NiTi material model parameters; (4) parallel to point (3), identification of pareto-optimal NiTi material candidates of the TAV.

2.1. FE models of aortic root and TAV

Idealized FE models of the human aortic root, including a portion of the ascending aorta, the left ventricular outflow tract, the native aortic valve leaflets and calcifications, were created (Fig. 3A). Details about these models were extensively described in Carbonaro et al. (2021). Briefly, the models were characterized by an aortic annulus diameter of 24 mm, a diameter of the ascending aorta of 29.3 mm and a constant thickness of 1.5 mm and 0.5 mm for the aortic root and the leaflets, respectively. The following three aortic root scenarios were considered (Fig. 3A): one aortic root without calcifications (in the following referred to as healthy configuration) and two diseased aortic roots (in the following referred to as diseased I and diseased II configuration, respectively) presenting with different calcification patterns according to previous experimental findings (Thubrikar et al., 1986). The calcification patterns of diseased I and II configurations were characterized by an arc shape located

along the leaflets coaptation and along attachment line (Thubrikar et al., 1986), respectively, with thickness and volume values based on data from patients suffering from aortic stenosis (Pawade et al., 2018; Sturla et al., 2016). The mechanical behavior of the aortic root and leaflets was described using an isotropic, incompressible hyperelastic Mooney-Rivlin material model (Auricchio et al., 2011; Gunning et al., 2014), while calcium deposits were modelled adopting an elasto-plastic material model with perfect plasticity (Bosi et al., 2018). The aortic root and the leaflets were meshed with 19,840 and 3,568 four-node shell elements with reduced integration S4R, respectively, assuming them as thin structures with a constant thickness (Bosi et al., 2018; Carbonaro et al., 2021). The calcium deposits were discretized with 23,266 and 35,967 four-node tetrahedral elements C3D4 in the case of diseased I and II configurations, respectively (Carbonaro et al., 2021). The mesh size was based on a previous grid independence study (Carbonaro et al., 2021). Tied contact was modeled between leaflets and the aortic root, as well as between leaflets and calcium deposits (Bosi et al., 2018; Carbonaro et al., 2021; Ovcharenko et al., 2016).

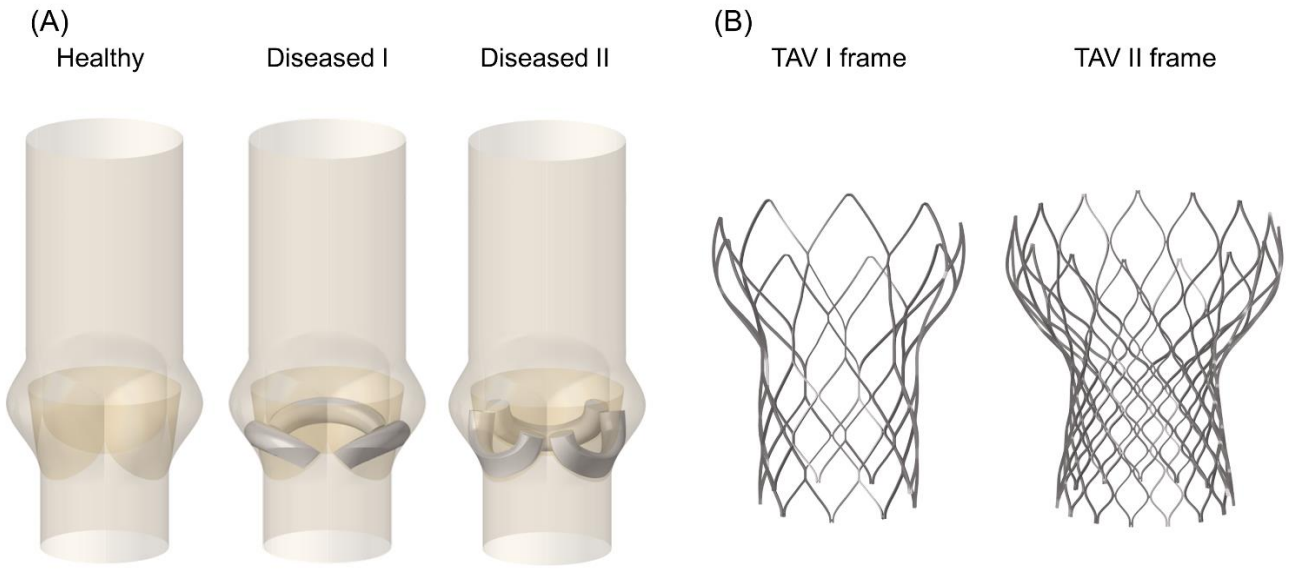


Fig. 3. FE models of human aortic root and TAV frame. (A) Three idealized aortic root scenarios referred to as healthy (without calcium deposits), diseased I and diseased II (with calcium deposits according to the calcium patterns identified in Thubrikar et al. (1986)); (B) Two TAV frames resembling different commercial devices: TAV I and TAV II.

FE element models of two TAV devices were developed (Fig. 3B). First, a model resembling the 27 mm Portico TAV (Abbott, Abbott Park, IL, USA) (Fig. 3B), in the following referred to as TAV I, was created using Hypermesh (Altair Engineering, Troy, MI, USA) in conjunction with Abaqus/Standard (Dassault Systèmes Simulia Corp.) by retrieving shape and dimensions from the manufacturer datasheet. The TAV model was simplified by considering only the NiTi frame and excluding the prosthetic leaflets, which have a negligible structural role (Bailey et al., 2016). Second, a model resembling the 29 mm CoreValve TAV (Medtronic, Dublin, Ireland) (Fig. 3B), in the following referred to as TAV II, was created as previously described (Carbonaro et al., 2021). The sizes of the 27 mm Portico and of the 29 mm CoreValve are recommended by the manufacturers for aortic annuli in the range of [23 mm, 25 mm] and of [23 mm, 26 mm], respectively. Therefore, they were compatible with the three idealized aortic root models considered in this study. Both TAV frames were meshed using B31 Timoshenko beam elements with properly oriented cross-sections, with a total number of 2,110 and 855 elements, respectively for the TAV I and II models, based on a previous mesh independence study (Carbonaro et al., 2021). A super-elastic constitutive model (Auricchio and Taylor, 1997) was implemented in Abaqus (Dassault Systèmes Simulia Corp.) to describe the mechanical behavior of the NiTi alloy. Details on the NiTi material model parameters are described in section 2.3.

2.2. FE analyses of TAV implantation

Non-linear FE analyses of the TAV implantation procedure were performed using the implicit FE solver Abaqus/Standard (Dassault Systèmes Simulia Corp.) on six computing cores of a workstation equipped with Intel® Core™ i7-8700 and 32 GB RAM. Details about the boundary conditions and solver parameters were extensively described elsewhere (Carbonaro et al., 2021). Interactions between the parts were implemented by considering the “hard” normal contact behavior with a friction coefficient of 0.09 for the TAV frame/aortic root and TAV frame/catheter capsule interaction, and a

Post-print

friction coefficient of 0.36 for the frame/calcium and aortic root/calcium (McGee et al., 2019b). The TAV deployment simulation was divided in two steps (Carbonaro et al., 2021). The first step (crimping step) consists of the crimping of the TAV frame into the catheter capsule (Fig. 4A, B), modeled as two concentric rigid cylinders (Cabrera et al., 2017). More in detail, the external cylinder of the catheter is radially crimped, reducing the diameter from the value of 100 mm (Fig. 4A) to the value of 6 mm (Fig. 4B), and fixing the diameter of the internal cylinder to the value of 5 mm. In the second step (expansion step) the TAV frame is released within the aortic root (Fig. 4C, D). More in detail, the external cylinder of the catheter is released to its initial diameter and, accordingly, the device is retrieved from the catheter and expanded within the aortic root (Fig. 4D).

The following four different TAV deployment scenarios were investigated: (1) TAV I implanted in the healthy aortic root configuration; (2) TAV II implanted in the healthy aortic root configuration; (3) TAV I implanted in the diseased I aortic root configuration; (4) TAV I implanted in the diseased II aortic root configuration.

To assess the mechanical performance of the TAV, two outputs from the FE analysis of TAV implantation were considered: (1) pullout force magnitude, defined as the resultant of the nodal radial forces acting on all nodes of the TAV frame multiplied by their corresponding friction coefficient (McGee et al., 2019b; Mummert et al., 2013) when the device implantation is completed and considered as a measure of the risk of device migration (McGee et al., 2019b; Mummert et al., 2013); (2) peak value of the maximum principal stress within the aortic root and leaflets, considered as a measure of the risk of tissue damage (Wang et al., 2015). A pullout force magnitude of 6.5 N and a peak maximum principal stress of 2.5 MPa were considered, respectively, as lower limit to avoid the migration of the device (McGee et al., 2019b; Mummert et al., 2013) and as the upper limit to avoid the damage of the tissue (Wang et al., 2015).

Post-print

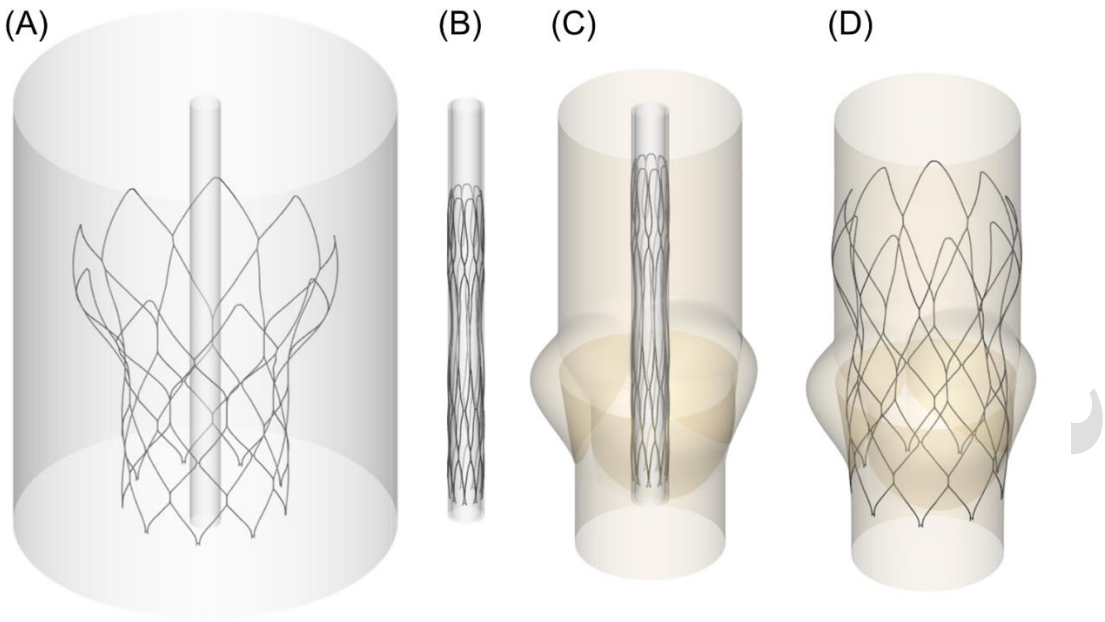


Fig. 4. FE analysis of the TAV deployment procedure. (A)–(B) TAV crimping into the catheter capsule (crimping step); (C)–(D) TAV expansion into the aortic root (expansion step).

2.3. Surrogate modelling

Surrogate models were constructed to define an approximate relationship between the NiTi super-elastic material model parameters and the two outputs of the FE analysis of TAV implantation for all the four deployment scenarios under investigation. Upper and lower bounds of the eight parameters of the NiTi constitutive model of Fig. 1 (Auricchio and Taylor 1997) were identified from the literature review summarized in Tables 1 and 2 and were reported in Table 3. In addition, a NiTi material (in the following referred to as median NiTi material) was defined considering for each material model parameter the median value from the ranges defined in Table 3. The modified extensible lattice sequence (MELS) sampling strategy (Hickernell et al., 2001) was implemented in Hyperstudy (Altair Engineering, Troy, MI, USA) to generate 60 sampling FE simulations of TAV implantation for each one of the four deployment scenarios under investigation (for a total number of

240 FE simulations). Fifty samples were used to develop the surrogate models (training dataset), the remaining ten samples were adopted for validation purposes (validation dataset). The number of samples N_{MELS} used in the MELS strategy to train the surrogate models was set according to the following equation:

$$N_{MELS} = 1.1(N+1)\frac{N+1}{2} \quad (1)$$

where N is the number of parameters of the constitutive material model (N = 8). Additionally, the following constraints were applied to the MELS sampling scheme to avoid unrealistic parameters combinations (see Fig. 1):

$$\begin{cases} \sigma_{tL}^{E} > \sigma_{tL}^{S} \\ \sigma_{tU}^{S} > \sigma_{tU}^{E} \\ \sigma_{tL}^{S} > \sigma_{tU}^{S} \end{cases} \quad (2)$$

The combinations of the eight material model parameters associated to the simulation samples are reported in Table S1 of the Supplementary material. On the performed 240 FE simulations, pullout force magnitude and peak maximum principal stress were computed. Gauss process surrogate models (Rasmussen and Williams, 2018) were developed in Matlab environment (Mathworks, Natick, MA, USA) to identify an approximate relationship between the eight NiTi material model parameters and pullout force magnitude and peak maximum principal stress values. The validity of the surrogate models was assessed by considering both the training and the validation dataset. Technically, the leave-one-out method was applied to the training data set, plotting each value predicted by the surrogate model as a function of the simulated value, and expressing the overall validation error in terms of predicted coefficient of determination R_{pred}^2 (Carbonaro et al., 2021; Corti et al., 2022). A consistency check was also performed by verifying that computed standardized cross validated residual (SCVR) values laid within the [-3, 3] range (Jones et al., 1998; Pant et al., 2012). Furthermore, the predicted values were plotted in function of the corresponding simulated values for the samples of the validation

Post-print

data set, quantifying the predicted coefficient of determination R^2_{pred} (Carbonaro et al., 2021; Corti et al., 2022).

Table 3. Lower, median and upper values of the parameters of the NiTi super-elastic material model of Auricchio and Taylor (1997). The lower and upper bounds of the parameters were identified from the literature review summarized in Tables 1 and 2.

NiTi material model parameter	Lower bound	Upper bound	Median value
E_A (MPa)	44000	88000	66000
E_M (MPa)	18358	50000	34179
ε^L	0.0405	0.0950	0.0678
σ^S_{tL} (MPa)	300	730	515
σ^E_{tL} (MPa)	345	850	597.5
σ^S_{tU} (MPa)	150	440	295
σ^E_{tU}(MPa)	50	410	230
σ^S_{cL} (MPa)	330	900	615

E_A: austenite elastic modulus, E_M: martensite elastic modulus, ε^L: uniaxial transformation strain, σ^S_{tL}: starting stress of transformation in traction loading, σ^E_{tL}: ending stress of transformation in traction loading, σ^S_{tU}: starting stress of reverse transformation in traction unloading, σ^E_{tU}: ending stress of reverse transformation in traction unloading, σ^S_{cL}: starting stress of transformation in compression loading.

2.4. Sensitivity analysis

The impact of the NiTi super-elastic characteristics on the TAV mechanical performance was investigated by performing both a multi- and a mono-parametric sensitivity analysis of the NiTi model parameters with respect to the FE outputs. First, a multi-parametric approach was proposed to investigate the correlation between the NiTi material model parameters and the FE outputs.

Post-print

Specifically, validated surrogate models were used to predict the FE outputs for each possible combination of material model parameters within a discretized parameter space (eight parameters and 10 samples within each parameter range). Partial rank correlation coefficients (PRCCs) were computed to measure the correlations among the eight material model parameters and the two FE outputs (Corti et al., 2022, 2020; Marino et al., 2008). Statistically significant correlations were assumed for p-value < 0.05. Second, a mono-parametric sensitivity study was conducted, with reference to the parameters exhibiting at least a week correlation (i.e., correlation coefficients at least higher than 0.30) with the FE outputs. Validated surrogate models were used to plot the FE outputs as a function of the material model parameters, by varying one parameter at time while maintaining all the others fixed at the median value, complying with the constraints of Eq. (2).

2.3. Multi-objective optimization

The optimization of the mechanical performance of the TAV device and the associated procedural effectiveness consisted in the minimization of both the risk of migration and tissue damage, and, therefore, involved the maximization of the pullout force magnitude and the minimization of the peak maximum principal stress within the aortic root. Accordingly, a multi-objective optimization analysis was conducted to identify sets of pareto-optimal material candidates for the two conflicting FE outputs. With regards to the adopted approach, the non-dominated sorting genetic algorithm (NSGA-II) (Deb et al., 2002) was used in Matlab, by setting a population size of 200, a binary tournament selection, a 0.8 crossover fraction and a Gaussian mutation (Carbonaro et al., 2021). The multi-objective optimization problem can be mathematically summarized as follows:

Post-print

$$\begin{cases} \max\limits_{\boldsymbol{x} \in D} pullout\ force\ (\boldsymbol{x}) \\ \min\limits_{\boldsymbol{x} \in D} peak\ maximum\ principal\ stress\ (\boldsymbol{x}) \\ s.t.: \begin{cases} \sigma_{tL}^{E} > \sigma_{tL}^{S} \\ \sigma_{tU}^{S} > \sigma_{tU}^{E} \\ \sigma_{tL}^{S} > \sigma_{tU}^{S} \\ D = \left\{ \begin{array}{l} \boldsymbol{x} = [E_A, E_M, \varepsilon^L, \sigma_{tL}^{S}, \sigma_{tL}^{E}, \sigma_{tU}^{S}, \sigma_{tU}^{E}, \sigma_{cL}^{S}]: \\ E_A \in [44GPa, 88GPa], E_M \in [18.4GPa, 50GPa] \\ \varepsilon^L \in [0.0405, 0.095], \sigma_{tL}^{S} \in [300MPa, 730MPa] \\ \sigma_{tL}^{E} \in [345MPa, 850MPa], \sigma_{UL}^{E} \in [150MPa, 440MPa] \\ \sigma_{tU}^{S} \in [50MPa, 410MPa], \sigma_{cL}^{S} \in [330MPa, 900MPa] \end{array} \right\} \end{cases} \end{cases} \quad (3)$$

3. Results

3.1 FE outputs (median NiTi material)

Within this section the median NiTi material model parameters were considered in the FE simulations to investigate the effects of the TAV frame geometry and aortic root scenario on the device mechanical performance.

Fig. 5 displays the main simulation results for the four TAV deployment scenarios under analysis. Both in TAV I and TAV II, in the case of the healthy aortic root configuration (Fig. 5A, B), nodal radial forces were mostly exchanged between the TAV frames and the left ventricular outflow tract. The total pullout force magnitude generated by TAV II was higher than that generated by TAV I (2.5 N *vs.* 1.0 N, respectively). The peak maximum principal stress within the aortic root was higher in the case of TAV II compared to TAV I (0.63 MPa *vs.* 0.29 MPa, respectively). Considering TAV I implanted in the diseased aortic root configurations (Fig. 5C, D), radial forces were mostly exerted between the TAV frame and the calcium deposits. This resulted in pullout force magnitudes for the diseased aortic root configurations higher than the healthy one (6.0 N and 6.1 N *vs.* 1.0 N, for diseased

Post-print

I, diseased II and healthy configurations, respectively). The peak maximum principal stress within the aortic root was higher with the presence of calcium deposits (0.75 MPa and 0.76 MPa *vs.* 0.29 MPa for diseased I, diseased II and healthy configurations, respectively).

Fig. 6 displays the force-displacement curves (expressed in terms of radial force magnitude *vs.* catheter diameter) of the four TAV deployment scenarios. The curves show a hysteresis loop, as typically occurs in NiTi devices. According to the NiTi material characteristics (refer to Fig. 1 for the typical stress-strain hysteresis curve of NiTi), large portions of the TAVs entered the transformation plateau during the crimping step and, as a result, higher radial force magnitude values were generated in the crimping step compared to the expansion step (Fig. 6). A change in slope was observable at the end of the expansion step (Fig. 6) and was due to the contact of the TAV frame with the lower region of the aortic root (more precisely, with the left ventricular outflow tract for the healthy configuration and with the calcific deposits for the diseased configurations), where the majority of nodal radial forces were generated (Fig. 5). TAV II frame generated higher radial forces than TAV I frame throughout both the crimping and expansion steps. Given the presence of calcium deposits and the resulting lower expansion of the TAV structure, TAV I frame generated higher radial forces during the contact with the diseased aortic root configurations than with the healthy one.

With reference to the TAV devices, Fig. 7 displays the maximum principal stress values for all the nodes of the TAV frame as a function of the maximum principal strain. TAV II frame was subjected to higher stress and strain values compared to TAV I frame when implanted in the healthy aortic root (Fig. 7A, B). TAV I frame exhibited higher stress and strain values with the presence of calcium deposits (Fig. 7C, D) with respect to the healthy aortic root, in consequence of the lower expansion of the frame.

Post-print

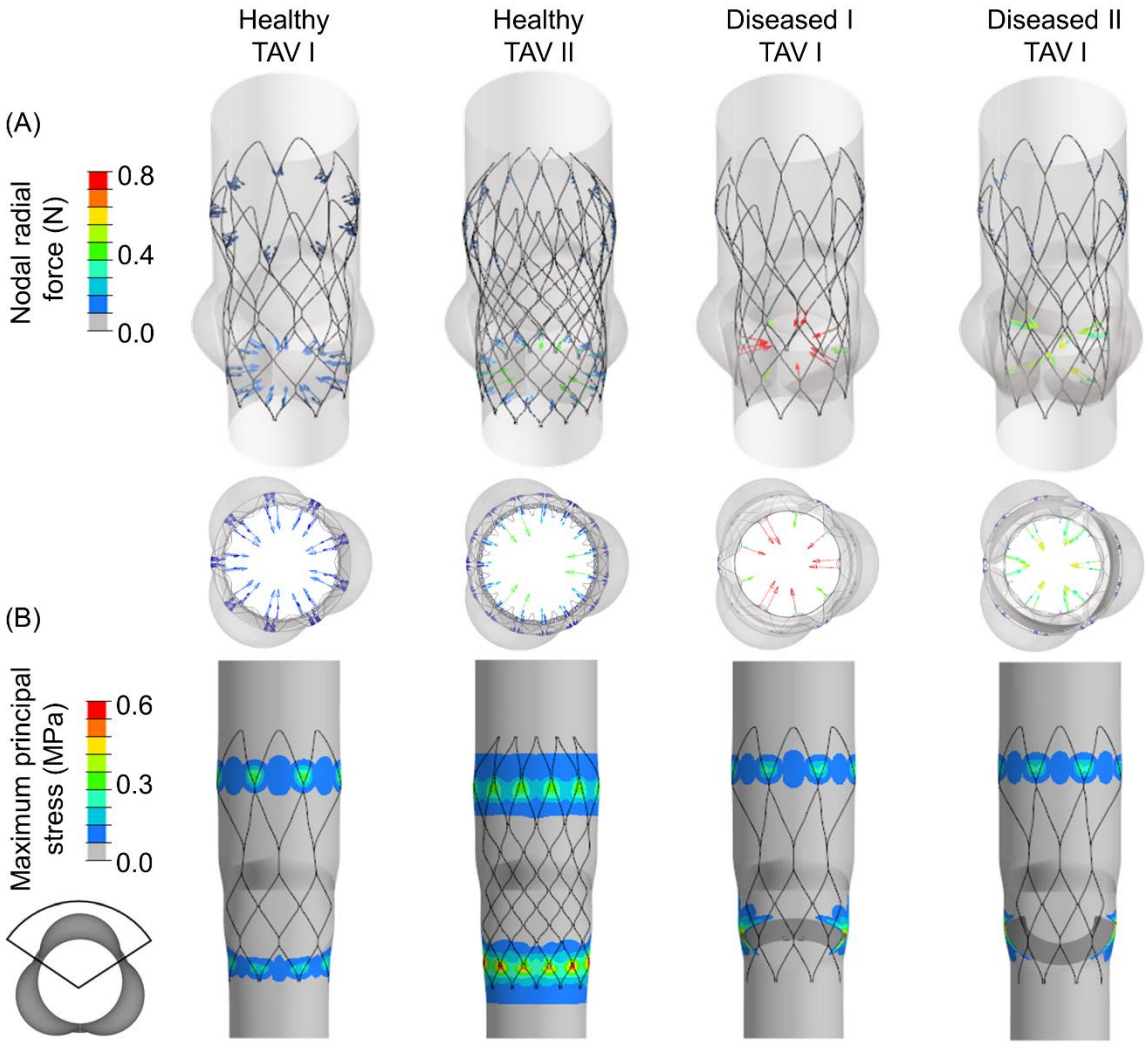


Fig. 5. Simulation results related to the two FE outputs in the case of median NiTi material for the four deployment scenarios, namely deployment of TAV I in healthy aortic root configuration, of TAV II in healthy aortic root configuration, of TAV I in diseased I aortic root configuration and of TAV I in diseased II aortic root configuration. (A) Radial nodal forces computed on the TAV frame. (B) Maximum principal stress computed within the aortic root wall.

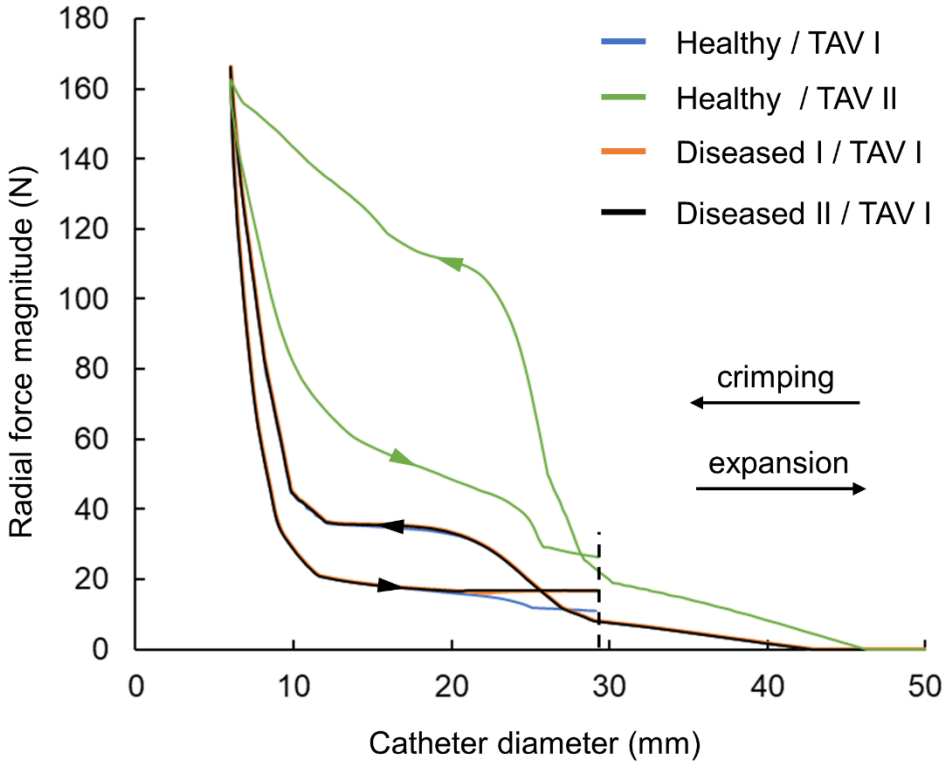


Fig. 6. Radial force magnitude exerted by the TAV as a function of the catheter diameter for the four deployment scenarios, namely deployment of TAV I in healthy aortic root configuration, of TAV II in healthy aortic root configuration, of TAV I in diseased I aortic root configuration and of TAV I in diseased II aortic root configuration. The curves were obtained analyzing both the steps of the FE analysis of TAV implantation, namely the crimping and the expansion up to the complete TAV apposition (occurring when the device goes in contact with the ascending aorta). The median NiTi material was considered for the TAV frame in all scenarios. The dotted line indicates the end of the TAV frame expansion within the aortic root.

Post-P

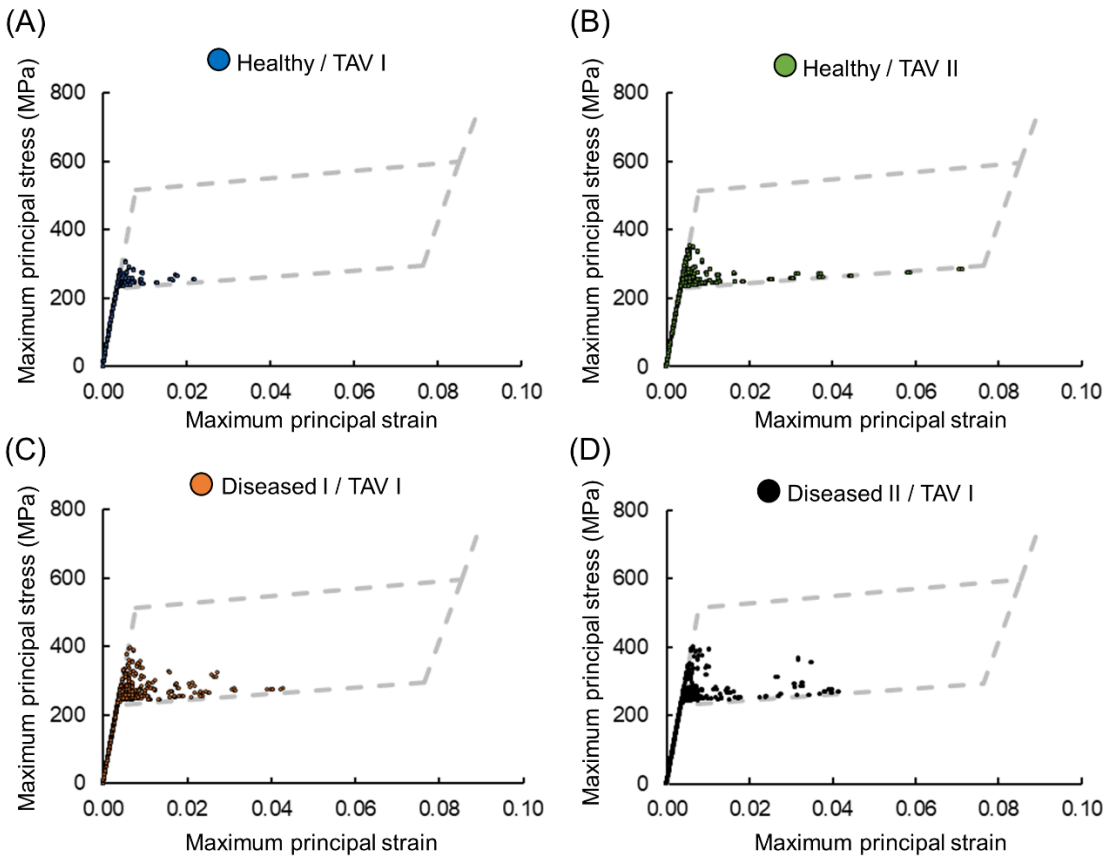


Fig. 7. Maximum principal stress as a function of the maximum principal strain for all the nodes of the TAVs, in the case of the median NiTi material. (A) TAV I deployed in the healthy aortic root configuration, (B) TAV II deployed in the healthy aortic root configuration, (C) TAV I deployed in the diseased I aortic root configuration and (D) TAV I deployed in the diseased II aortic root configuration. The tensile uniaxial stress *vs.* strain curve of the median material is indicated with a dotted line in grey.

3.2 Surrogate modelling

Fig. 8 presents pullout force magnitude and peak maximum principal stress values as obtained from the 60 simulation samples generated per each one of the four TAV deployment scenarios. The conflict between the two quantities of biomechanical interest clearly emerges independent of the

explored scenario, where high values of pullout force magnitude (Fig. 8A) correspond to high values of peak maximum principal stress (Fig. 8B): on one hand high values of pullout force magnitude could reduce the risk for TAV migration; on the other hand, they could lead to excessive peak maximum principal stress values, which are related to an increased risk of tissue damage (see Section 2.2). With reference to the healthy configuration, in accordance with the findings reported in Section 3.1 for the cases with the median NiTi material, TAV II frame presented higher values of both pullout force magnitude and peak maximum principal stress than TAV I frame. Moreover, the samples related to the healthy configuration presented, on average, pullout force magnitude and peak maximum principal stress values lower than those related to the diseased configurations.

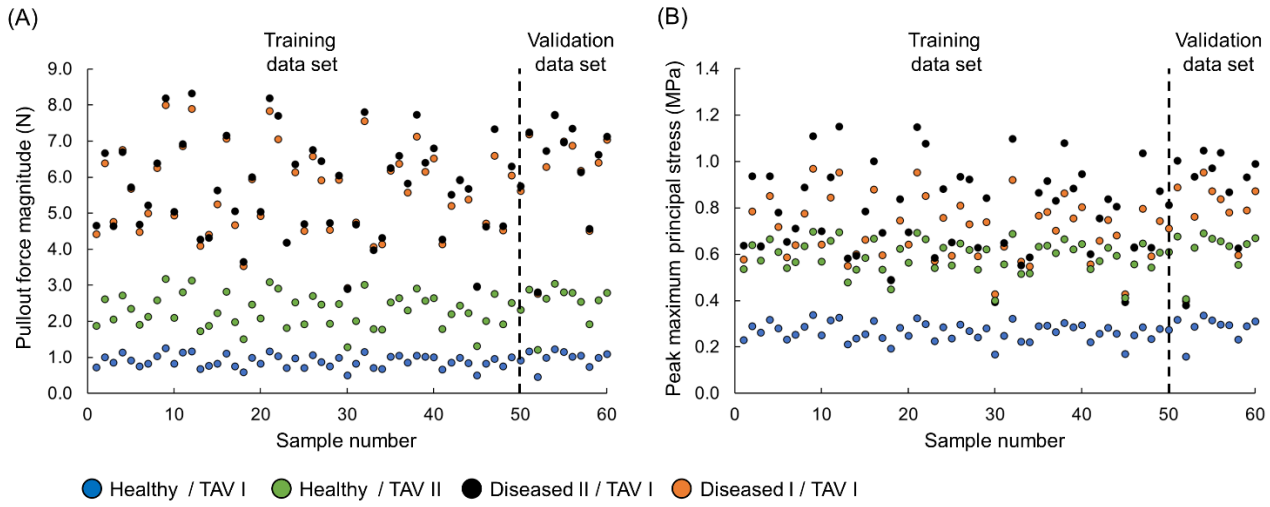


Fig. 8. FE outputs in terms of (A) pullout force magnitude and (B) peak maximum principal stress of the MELS sampling simulations for the four TAV deployment scenarios, namely deployment of TAV I in healthy aortic root configuration, of TAV II in healthy aortic root configuration, of TAV I in diseased I aortic root configuration and of TAV I in diseased II aortic root configuration. Samples 1 to 50 and 51 to 60 are related to the training and validation data sets, respectively.

Gauss process surrogate models of the pullout magnitude and peak maximum principal stress were generated based on MELS training dataset. The result of the surrogate modelling validation

process is presented in Fig. 9. An excellent agreement between the predicted and simulated biomechanical quantities was obtained for all the TAV deployment scenarios, as confirmed by the strong direct proportionality of the data samples (R^2_{pred} > 0.98). Moreover, nearly all SCVR values of the predicted pullout force magnitude and peak maximum principal stress laid within the required interval [−3, 3] (Fig. S1 of the Supplementary material), indicating the affordability of the adopted Gauss process surrogate modelling strategy (Pant et al., 2012). Additionally, with reference to the validation dataset, the consistency between the FE outputs predicted by the Gauss process against those obtained with FE simulations was confirmed by the high values of the coefficients of determination (R^2_{pred} > 0.98) computed for the validation samples (Fig. S2 of the Supplementary material).

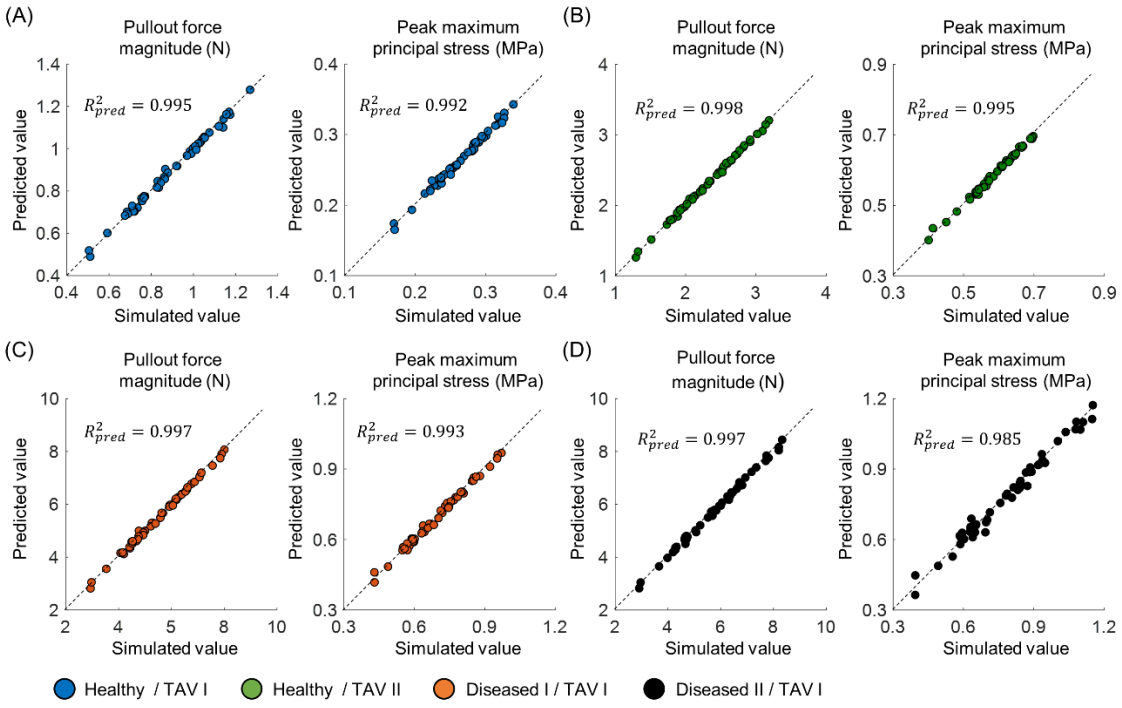


Fig. 9. Leave-one-out predicted values of the pullout force magnitude and peak maximum principal stress in function of the corresponding simulated values, in the case of (A) TAV I deployed in the healthy aortic root configuration, (B) TAV II deployed in the healthy aortic root configuration, (C) TAV I deployed in the diseased I aortic root configuration and (D) TAV I deployed in the diseased II aortic root configuration.

3.3 Sensitivity analysis

3.3.1 Multi-parametric sensitivity analysis

The values of PRCCs between each NiTi material model parameter and (1) pullout force magnitudes and (2) peak maximum principal stresses (Fig. 10) highlighted that five out of eight of the parameters (E_A, σ_{tL}^S, σ_{tU}^S, σ_{tU}^E and σ_{cL}^S) were significantly associated with both the FE outputs and for all the four TAV deployment scenarios (correlation coefficients at least higher than 0.3). In detail: E_A exhibited a moderate to strong and a weak to strong positive correlation to the pullout force magnitude (Fig 10A) and peak maximum principal stress (Fig 10B), respectively; σ_{tL}^S exhibited a moderate negative correlation to both the biomechanical quantities; σ_{tU}^S, σ_{tU}^E and σ_{cL}^S exhibited a strong to very strong positive correlation to both the biomechanical quantities. Conversely, the remaining NiTi material model parameters E_M, ε^L and σ_{tL}^S presented significant correlations with just few of the TAV deployment scenarios, and a very weak correlation with both the biomechanical quantities of interest. Finally, it emerged from Fig. 10 that the TAV frame geometry and the anatomy of the aortic root had a marginal effect on the correlation between the material model parameters and the two biomechanical quantities, with the exception of E_A and peak maximum principal stress (Fig 10B).

Post-print

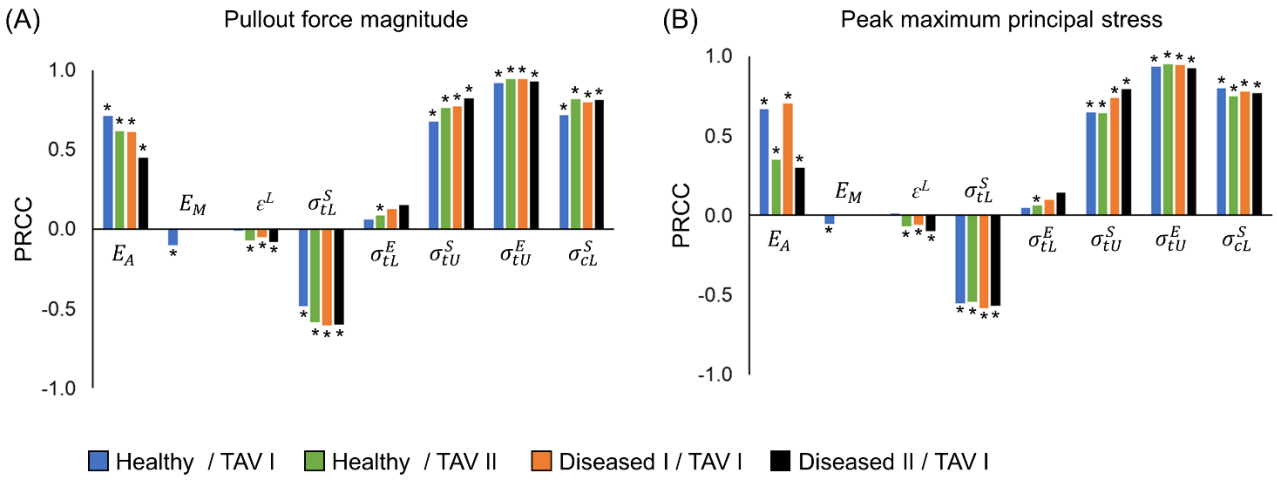


Fig. 10. Partial rank correlation coefficients (PRCCs) between each one of the eight NiTi super-elastic material model parameters and the (A) pullout force magnitude and (B) peak maximum principal stress, for the four investigated deployment scenarios, namely deployment of TAV I in healthy aortic root configuration, of TAV II in healthy aortic root configuration, of TAV I in diseased I aortic root configuration and of TAV I in diseased II aortic root configuration. (*) Significant PRCC, p-value < 0.05.

3.3.2 Mono-parametric sensitivity analysis

With reference to the five NiTi material model parameters E_A, σ^S_{tL}, σ^S_{tU}, σ^E_{tU} and σ^S_{cL} significantly correlated to both pullout force magnitude and peak maximum principal stress, validated surrogate models were adopted to investigate the impact of each single parameter on the TAV mechanical performance. The curves of the pullout force magnitude and peak maximum principal stress obtained by varying one parameter at a time while maintaining the others fixed at the median value are presented in Fig. 11. In accordance with Fig. 10, a similar trend of the biomechanical quantities of interest is observable for the four TAV deployment scenarios. In detail, pullout force magnitudes and peak maximum principal stresses are monotonically increasing with E_A, σ^S_{tU}, σ^E_{tU}, σ^S_{cL} and decreasing with σ^S_{tL}, respectively. Furthermore, the highest pullout force magnitude and peak maximum principal stress

values were observed for the two diseased aortic root configurations (compared to the healthy one) and for the case of TAV II (compared to TAV I).

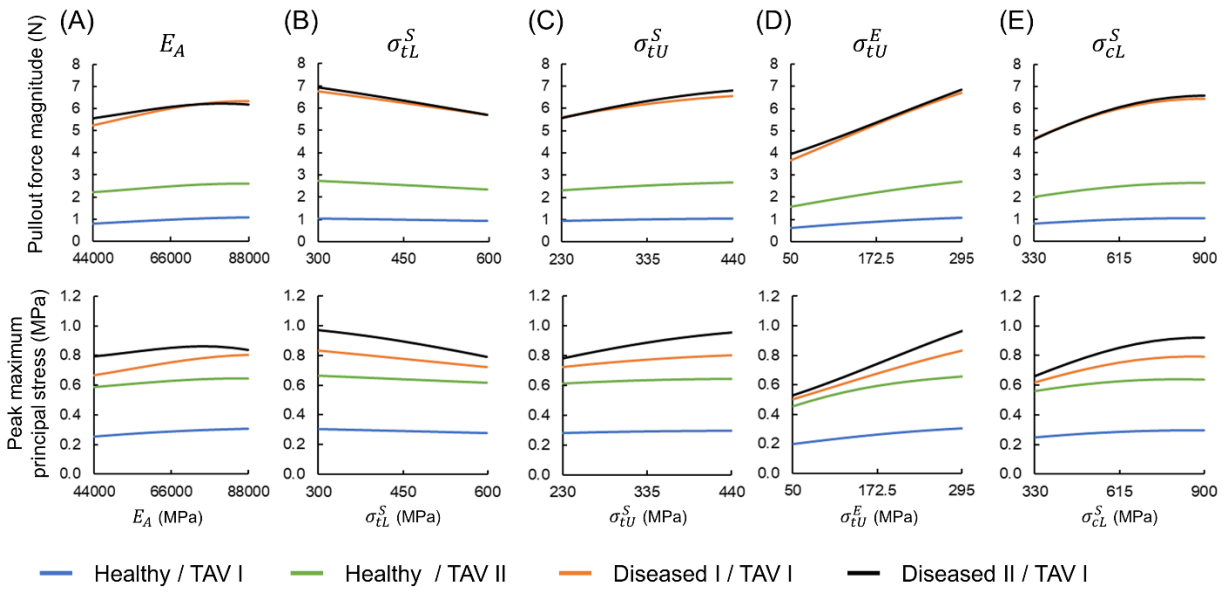


Fig. 11. Curves of the pullout force magnitude and peak maximum principal stress obtained by varying one material model parameters at a time while maintaining the others fixed at the median value, with consideration of the parameter constraints in Eq. (2). The parameters with a strong correlation to the two FE outputs were considered, i.e. (A) E_A, (B) σ_{tL}^S, (C) σ_{tU}^S,(D) σ_{tU}^E and (E) σ_{cL}^S (see Fig. 1).

3.4 Multi-objective optimization

Fig. 12 depicts the sets of non-dominated optimal solutions lying on the Pareto front of the two conflicting biomechanical quantities characterizing the mechanical performance of TAVs. A marked difference of the ranges of values of the Pareto front emerged between TAV I (Fig. 12A) and TAV II (Fig. 12B) as well as between the healthy (Fig. 12A, B) and the diseased aortic root configurations (Fig. 12C, D). For each of the four TAV deployment scenarios, two NiTi material candidates were selected at the extremities of the Pareto front (points 1 to 8 in Fig. 12). The values of pullout force

Post-print

magnitude and peak maximum principal stress of the selected NiTi material candidates and the corresponding values of the optimal material model parameters are reported in Table 4.

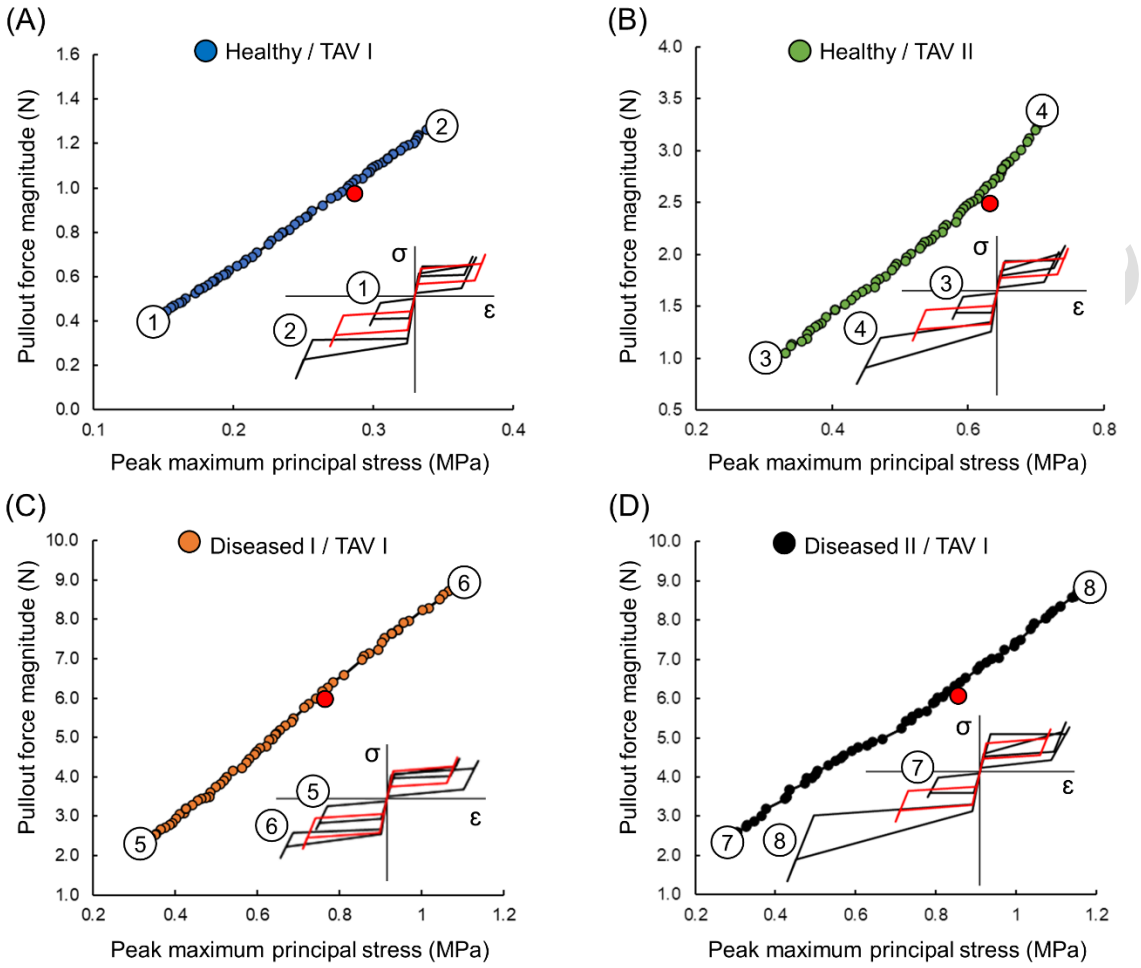


Fig. 12. Pareto optimal material solutions of the two FE outputs in the case of (A) TAV I deployed in the healthy aortic configuration, (B) TAV II deployed in the healthy aortic root configuration, (C) TAV I deployed in the diseased I aortic root configuration and (D) TAV I deployed in the diseased II aortic root configuration. Two optimal NiTi material candidates (i.e., points 1 to 8) were selected at the extremities of each Pareto front. The point associated with the median NiTi material is displayed in red for each deployment scenario. The super-elastic uniaxial stress *vs.* strain curves are illustrated for the median material, in red, and for eight optimal NiTi material candidates, in black.

Accepted manuscript at https://linkinghub.elsevier.com/retrieve/pii/S1751-6161(22)00528-8

Table 4. Values of the NiTi material model parameters and FE outputs of the eight selected pareto-optimal material candidates.

	Healthy / TAV I		Healthy / TAV II		Diseased I / TAV I		Diseased II / TAV I	
	NiTi 1	NiTi 2	NiTi 3	NiTi 4	NiTi 5	NiTi 6	NiTi 7	NiTi 8
E_A (MPa)	56391	85119	72464	86335.95	49160	80553	48482.47	73737.94
E_M (MPa)	30768	32345	29584	27681	28966	28590	25913.75	35094.63
ε^L	0.0548	0.0511	0.0915	0.0566	0.0922	0.0914	0.0832	0.0777
σ_{tL}^S (MPa)	545	416	550	361	466	412	676.87	328.67
σ_{tL}^E (MPa)	559	563	639	688	565	622	682.70	724.47
σ_{tU}^S (MPa)	155	388	187	420	174	391	202.30	324.77
σ_{tU}^E (MPa)	56	373	54	277	51	350	63.09	290.37
σ_{cL}^S (MPa)	408	724	404	745	360	721	393.49	687.60
Pullout force magnitude (N)	0.39	1.28	1.05	3.34	2.35	8.86	2.33	8.85
Peak maximum principal stress (MPa)	0.14	0.35	0.33	0.72	0.33	1.08	0.27	1.18

E_A: austenite elastic modulus, E_M: martensite elastic modulus, ε^L: uniaxial transformation strain, σ_{tL}^S: starting stress of transformation in traction loading, σ_{tL}^E: ending stress of transformation in traction loading, σ_{tU}^S: starting stress of reverse transformation in traction unloading, σ_{tU}^E: ending stress of reverse transformation in traction unloading, σ_{cL}^S: starting stress of transformation in compression loading.

Post-print

4 Discussion

Continuous developments are made to TAV design (Howard et al., 2019; Wiegerinck et al., 2016) to improve the effectiveness and safety of the treatment and to extend TAV replacement procedure to younger and lower risk patients (Mack et al., 2019; Popma et al., 2019). Within this context, FE modelling is an elective tool to support the TAV design phase, enabling the optimization of the mechanical performance and, as a consequence, of the clinical outcomes (Dasi et al., 2017; Fanning et al., 2013). Previous computational studies (Barati et al., 2022, 2021; Carbonaro et al., 2021; Rocatello et al., 2019a) investigated the relation between geometrical attributes and mechanical performance of self-expandable TAVs, with the ultimate goal of identifying optimal TAV frame geometries. Differently, this study focuses on the material of the TAV frame, proposing a computational framework to analyze the impact of the NiTi super-elastic material properties on the TAV mechanical performance of the device and ultimately to optimize the NiTi material. As main findings of the study, it is reported that (1) only five out of eight NiTi material model parameters (E_A, σ_{tL}^S, σ_{tU}^S, σ_{tU}^E and σ_{cL}^S) were significantly associated with pullout force magnitude and peak maximum principal stress within the aortic root for all the TAV deployment scenarios (correlation coefficients at least higher than 0.3), and thus should be accounted for during the device design phase; (2) the TAV frame geometry and the anatomy of the aortic root had a marginal effect on the level of influence of each material model parameter; (3) the multi-objective optimization led to the identification of personalized NiTi alloys with pareto-optimal characteristics in terms of TAV mechanical performance.

4.1 FE model of TAV implantation

The evaluation of the force exerted by the implanted TAV to the surrounding tissue represents a precious, clinically relevant feedback of the postoperative response, as highlighted by the

Post-print

regulatory documentation (ISO, 2013) and medical community (Rotman et al., 2018). The results of the FE models of TAV implantation developed in this study satisfactorily agreed with data reported by the literature. In detail, TAV I frame (resembling the Portico TAV) exhibited lower values of pullout force magnitude compared to TAV II frame (resembling the CoreValve TAV) (Figs. 5, 6 and 8), in accordance with previously conducted *in vitro* and *in silico* studies (Finotello et al., 2021; Kumar et al., 2014). The overall behavior of the force-displacement curves of both TAV I and TAV II frames (Fig. 6) was comparable to that reported by Finotello et al., (2021), in which both Portico and CoreValve TAVs were experimentally and numerically investigated. The observed dependence of the generated pullout force magnitude values on the aortic root configuration (Figs. 5, 6 and 8) agreed well with previous findings (Wang et al., 2015, 2012) reporting higher values in the diseased aortic roots as compared to the healthy one. This is ascribable to the combined effect of the adopted value of friction coefficient between the TAV frame and the calcium deposits (McGee et al., 2019b; Mummert et al., 2013), and to the reduced TAV frame expansion in the left ventricular outflow tract, due to the presence of calcifications in the diseased aortic root configurations (Fig. 5). Moreover, the values of peak maximum principal stress within the aortic wall (Figs. 5 and 8) reported a marked dependency on the presence of calcium deposits and were consistent with those computed in previous computational studies (Finotello et al., 2021; McGee et al., 2019a; Morganti et al., 2014; Sturla et al., 2016; Wang et al., 2015, 2012). The higher values of peak maximum principal stress that were found in the diseased aortic root configurations as compared to the healthy one are ascribable by the calcium deposits that were pushed by the TAV frame against the aortic root wall (Fig. 5).

4.2 NiTi material model parameters: sensitivity analysis

The mechanical properties of NiTi are strongly dependent on the chemical composition of the alloy, on the grain size and distribution, and on the specific metallurgical processing provided by each

Post-print

manufacturer (Duerig et al., 2000; Henderson et al., 2011; Hodgson and Russell, 2000; Liu and Mishnaevsky, 2013; Mwangi et al., 2019; Nemat-Nasser and Guo, 2006; Valiev et al., 2020). Indeed, in order to obtain the Conformitè Europëenne (CE) mark and/or Food and Drug Administration approval, regulatory agencies request TAV manufacturers to experimentally test the adopted NiTi alloy and to provide accurate data of its super-elastic behavior, evaluating the stress of the upper and lower plateau in tension (ASTM, 2013; FDA, 2020; ISO, 2013). The high variability of the fabricated NiTi material properties was reflected in the wide range of the material model parameter values used in the computational structural studies on self-expandable TAVs (Table 2). In this regard, previous computational studies (Cabrera et al., 2017; Finotello et al., 2021) compared the mechanical response of the TAV frame considering different parameter values for the NiTi alloys constitutive model, reporting marked differences in terms of both radial force and stress within the aortic wall. To complement the previous studies, here multi- and mono-parametric sensitivity analyses were conducted to investigate the effect that each NiTi material model parameter has on the TAV mechanical performance.

Table 5 provides the interpretation of the results of the multi-parametric sensitivity analysis for each NiTi material model parameter. In detail, material model parameters related to the tensile behavior (E_A, σ_{tL}^S, σ_{tU}^S, σ_{tU}^E and σ_{cL}^S) and the parameter σ_{cL}^S related to the compression behavior were correlated with the FE simulation outputs in all the four scenarios. All these model parameters should be carefully considered during the design phase as they could significantly affect the mechanical response of the TAV frame. In this regard, it must be recalled that the mechanical performance of the TAV frame depends on the whole loading history of NiTi. Specifically, the TAV implantation is a displacement-controlled procedure (Fig. 4), in which the TAV frame is loaded (crimping step) and unloaded (expansion step). The stress and strain values of the TAV frame increase during the crimping-loading phase and decrease during the expansion-unloading phase to the values reported in Fig. 7, when the

Post-print

device is completely deployed. Accordingly, the overall higher values of stress of the TAV frame correspond to a higher pullout force magnitude and, therefore, to a higher peak maximum principal stress within the aortic wall. Considering that the FE simulation outputs were evaluated at the end of the expansion step, when the TAV expansion is completed, the material model parameters related to the unloading part of the NiTi super-elastic curve (i.e., σ_{tU}^{S}, σ_{tU}^{E} and σ_{cL}^{S}) exhibited the strongest impact on the mechanical performance of the TAV frame. Moreover, it should be noticed that the parameter σ_{cL}^{S} is crucial when dealing with TAV frames, whose structure is mainly subjected to bending loads when radially crimped within the catheter.

Although based on few deployment scenarios, the results of the multi-parametric analysis revealed also that the TAV frame geometry and the anatomy of the aortic root have a marginal effect on the level of influence of each material model parameter on the pullout force magnitude and peak maximum principal stress within the aortic root. This result suggests that the TAV manufacturers could evaluate the impact of different materials provided by the NiTi suppliers, each with a unique super-elastic characteristic behavior, focusing mainly on the TAV mechanical performance rather than on the TAV frame geometry and anatomy of the implantation site.

In addition to the multi-parametric analysis, a mono-parametric sensitivity analysis was conducted herein to investigate the impact of the single material model parameters on the FE simulation output. The results of this analysis were related to the specific TAV device and aortic root configuration, providing quantitative information on the impact of each single NiTi material model parameter maintaining the others at the median value. Hence, the reported results (Fig. 11) and, more in general, the proposed computational framework could guide TAV manufacturers during the device design phase, providing valuable information on the relation between the super-elastic characteristics of the supplied NiTi alloys and the device mechanical response.

Post-print

Table 5. Explanation of the impact of each NiTi material model parameter on the TAV mechanical performance. The correlation to the FE outputs is related to the multi-parametric sensitivity analysis based on the calculation of the PRCCs. For a better interpretation of the table, the reader is referred to Figs. 1 and 7, reporting the NiTi material model parameters and the maximum principal stress as a function of the maximum principal strain within the TAV frames, respectively.

NiTi material model parameter	Correlation to the FE outputs	Interpretation
E_A	Significant, positive, weak to strong	A higher value results in a higher slope of the austenite linear elastic region, with consequent higher stress values of the TAV frame
E_M	Non-significant	Stress values of the TAV frame lie outside the martensite stability region at the end of the expansion step
ε^L	Non-significant	Negligible effect on the stress values of the TAV frame in the expansion step
σ_{tL}^S	Significant, negative, moderate	A lower value results in a larger portion of the TAV frame to enter the upper stress-strain plateau during the crimping step, with consequent higher stress at the end of the expansion step
σ_{tL}^E	Non-significant	Stress values of the TAV frame lie outside the martensite stability region at the end of the expansion step
σ_{tU}^S	Significant, positive, strong	A higher value results in higher stress values of the TAV frame during the expansion step
σ_{tU}^E	Significant, positive, very strong	A higher value results in higher stress values of the TAV frame during the expansion step
σ_{cL}^S	Significant, positive, strong	A higher value modifies the whole material compression behavior, resulting in higher stress values of the TAV frame in compression

E_A: austenite elastic modulus, E_M: martensite elastic modulus, ε^L: uniaxial transformation strain, σ_{tL}^S: starting stress of transformation in traction loading, σ_{tL}^E: ending stress of transformation in traction loading, σ_{tU}^S: starting stress of reverse transformation in traction unloading, σ_{tU}^E: ending stress of reverse transformation in traction unloading, σ_{cL}^S: starting stress of transformation in compression loading.

Post-print

4.3 Optimal NiTi material model parameters selection

A multi-objective optimization of the TAV mechanical response was also conducted, searching for NiTi material candidates within the whole material design/production space (see Eq. (3)). The optimization approach successfully led to the identification of pareto-optimal NiTi alloys, each with a distinct TAV mechanical performance and in turn with a distinct combination of super-elastic model parameters (Fig. 12). Considering the great effect of the chemical composition and metallurgical processing on the NiTi super-elastic behaviour, these personalized materials could be designed by the NiTi suppliers by appropriately tuning the thermo-mechanical processing parameters.

4.4 Limitations and future perspectives

This study presents some limitations that might weaken the effectiveness of the proposed computational framework. Idealized FE models of the aortic root and calcium deposits were considered in terms of geometry and material properties (Carbonaro et al., 2021). Moreover, the constitutive model used to describe the super-elastic material behaviour of NiTi (Auricchio and Taylor, 1997) is characterized by a simplified material compression behaviour and it is not capable to represent the inelastic deformations that are experimentally noticeable. In this context, investigations were conducted to develop more advanced NiTi constitutive models, including a higher number of material model parameters (Lagoudas et al., 2012; Petrini et al., 2017a). Nevertheless, the adopted constitutive model is widely used for both research and industry applications. In addition, the accessibility to uniaxial compression data is generally limited, due to structural instability issues of the slender specimens used for the experimental campaign (Henderson et al., 2011). Ultimately, due to the high computational costs, a limited number of deployment scenarios was accounted for. Providing a detailed analysis on the effects of the geometrical features of the TAV frame and anatomical characteristics of the aortic

Post-print

root was beyond the aims of this study. However, additional TAV frame geometries implanted in a wider range of aortic root anatomies could be considered to further support the findings here presented.

Despite the limitations, the proposed computational framework proved to be effective in investigating the impact of the material model parameters on the TAV mechanical performance, providing potential support to device design phase. Several advances could be implemented to further extend its potential. In detail, more consistent and a larger range of values of the NiTi material model parameters than that related to the computational studies on self-expandable TAVs (Tables 2 and 3) could be explored if specific information from NiTi suppliers were available. Additional aspects related to the TAV procedural effectiveness could be considered, including the assessment of paravalvular leakage (De Jaegere et al., 2016; Mao et al., 2018; Rocatello et al., 2019b) and thrombosis (Bianchi et al., 2019; Nappi et al., 2020), by coupling the FE analyses of TAV implantation with computational fluid dynamics simulations. Moreover, the proposed computational framework could be combined with a geometrical optimization platform (Barati et al., 2021; Carbonaro et al., 2021; Rocatello et al., 2019a), in order to further analyse the interaction between the TAV and the aortic root. Within this context, the computational framework could be also extended by coupling a NiTi manufacturing framework, which associates the thermo-mechanical processing parameters to the super-elastic characteristics, with the proposed multi-objective optimization approach. The implementation of such a framework would not only provide great benefits in terms of TAV performance and clinical effectiveness, but also in terms of times and costs related to the device design phase. Indeed, investigations could be conducted to develop self-expandable TAVs that fits to various aortic root dimensions, controlling the mechanical response without changing the TAV frame geometry, by only tuning the NiTi super-elastic characteristics in relation to the anatomy in which the device is implanted. Finally, considering the numerous applications of NiTi in the cardiovascular field and the increasing interest towards its adoption as a medical grade material (Mwangi et al., 2019), the current

Post-print

computational framework shows enough flexibility to be extended to self-expandable intravascular stents and other implantable cardiovascular devices.

5 Conclusions

In this work, a computational framework based on FE modelling, surrogate modelling and optimization process was developed for the evaluation of the impact of the NiTi super-elastic material model parameters on the TAV mechanical performance. The framework was applied to two different TAV frame designs and three idealized aortic root configurations, with and without calcium deposits. The findings of the study showed that, according to the widely adopted NiTi constitutive model by Auricchio and Taylor (1997), only five out of the eight material model parameters were significantly correlated with pullout force magnitude and peak maximum principal stress within the aortic root in all the investigated scenarios and should be taken into consideration during the device design phase. Furthermore, the results highlighted that the impact of those material model parameters on the TAV mechanical response was independent from the TAV frame geometry and the anatomy of the aortic root. Finally, multi-objective optimization was applied, leading to the definition of personalized NiTi alloys with optimized characteristics in terms of TAVs mechanical response and procedural outcomes. Overall, the study demonstrated that *in silico* modelling based on FE method confirmed to be an effective tool to support the TAV design phase, enabling here to investigate the role of the material on the device mechanical performance. The proposed computational framework provided enough flexibility to be extended to other implantable NiTi-based cardiovascular devices and to integrate additional features, including NiTi manufacturing information and geometrical optimization.

Post-print

Accepted manuscript at https://linkinghub.elsevier.com/retrieve/pii/S1751-6161(22)00528-8

CRediT authorship contribution statement

D. Carbonaro: Conceptualization, Methodology, Investigation, Validation, Formal analysis, Visualization, Data curation, Writing – original draft, Writing – Review & Editing. **S. Zambon**: Methodology, Writing – Review & Editing. **A. Corti**: Formal analysis, Writing – Review & Editing. **D. Gallo**: Conceptualization, Writing – Review & Editing. **U. Morbiducci**: Conceptualization, Supervision, Funding acquisition, Writing – Review & Editing. **A. Audenino**: Conceptualization, Supervision, Funding acquisition, Writing – Review & Editing. **C. Chiastra**: Conceptualization, Methodology, Supervision, Project administration, Writing – original draft, Writing – Review & Editing.

Declaration of competing interest

The authors declare that they have no known competing financial interests or personal relationships that could have appeared to influence the work reported in this paper.

Funding

This work has been supported by the Italian Ministry of Education, University and Research (FISR2019_03221, CECOMES) and by the Piedmont Region, Italy (POR FESR PiTeF 2014-20 351-96, Nitiliera).

Acknowledgements

None.

Post-print

References

ASTM, 2013. Standard specification for wrought Nickel-Titanium shape memory alloys for medical devices and surgical implants, ASTM F2633 − 13.

Auricchio, F., Conti, M., Morganti, S., Totaro, P., 2011. A computational tool to support pre-operative planning of stentless aortic valve implant. Med. Eng. Phys. 33, 1183–1192. https://doi.org/10.1016/j.medengphy.2011.05.006

Auricchio, F., Taylor, R.L., 1997. Shape-memory alloys: modelling and numerical simulations of the finite-strain superelastic behavior. Comput. Methods Appl. Mech. Eng. 143, 175–194. https://doi.org/10.1016/S0045-7825(96)01147-4

Bailey, J., Curzen, N., Bressloff, N.W., 2016. Assessing the impact of including leaflets in the simulation of TAVI deployment into a patient-specific aortic root. Comput. Methods Biomech. Biomed. Engin. 19, 733–744. https://doi.org/10.1080/10255842.2015.1058928

Barati, S., Fatouraee, N., Nabaei, M., Berti, F., Petrini, L., Migliavacca, F., Rodriguez Matas, J.F., 2021. A computational optimization study of a self-expandable transcatheter aortic valve. Comput. Biol. Med. 139, 104942. https://doi.org/10.1016/j.compbiomed.2021.104942

Barati, S., Fatouraee, N., Nabaei, M., Petrini, L., Migliavacca, F., Luraghi, G., Felix, J., Matas, R., 2022. Patient-specific multi-scale design optimization of transcatheter aortic valve stents. Comput. Methods Programs Biomed. 221, 106912. https://doi.org/10.1016/j.cmpb.2022.106912

Berti, F., Bridio, S., Luraghi, G., Pant, S., Allegretti, D., Pennati, G., Petrini, L., 2022. Reliable Numerical Models of Nickel-Titanium Stents: How to Deduce the Specific Material Properties from Testing Real Devices. Ann. Biomed. Eng. 50, 467–481. https://doi.org/10.1007/s10439-022-02932-1

Bianchi, M., Marom, G., Ghosh, R.P., Rotman, O.M., Parikh, P., Gruberg, L., Bluestein, D., 2019.

Post-print

Patient-specific simulation of transcatheter aortic valve replacement: Impact of deployment options on paravalvular leakage. Biomech. Model. Mechanobiol. 18, 435–451. https://doi.org/10.1007/s10237-018-1094-8

Bosi, G.M., Capelli, C., Cheang, M.H., Delahunty, N., Mullen, M., Taylor, A.M., Schievano, S., 2020. A validated computational framework to predict outcomes in TAVI. Sci. Rep. 10, 1–11. https://doi.org/10.1038/s41598-020-66899-6

Bosi, G.M., Capelli, C., Cheang, M.H., Delahunty, N., Mullen, M., Taylor, A.M., Schievano, S., 2018. Population-specific material properties of the implantation site for transcatheter aortic valve replacement finite element simulations. J. Biomech. 71, 236–244. https://doi.org/10.1016/j.jbiomech.2018.02.017

Bosi, G.M., Capelli, C., Khambadkone, S., Taylor, A.M., Schievano, S., 2015. Patient-specific finite element models to support clinical decisions: A lesson learnt from a case study of percutaneous pulmonary valve implantation. Catheter. Cardiovasc. Interv. 86, 1120–1130. https://doi.org/10.1002/ccd.25944

Bosmans, B., Famaey, N., Verhoelst, E., Bosmans, J., Vander Sloten, J., 2016. A validated methodology for patient specific computational modeling of self-expandable transcatheter aortic valve implantation. J. Biomech. 49, 2824–2830. https://doi.org/10.1016/j.jbiomech.2016.06.024

Cabrera, M.S., Oomens, C.W.J., Baaijens, F.P.T., 2017. Understanding the requirements of self-expandable stents for heart valve replacement: Radial force, hoop force and equilibrium. J. Mech. Behav. Biomed. Mater. 68, 252–264. https://doi.org/10.1016/j.jmbbm.2017.02.006

Carbonaro, D., Chiastra, C., Morbiducci, U., Audenino, A., 2020. Transcatheter aortic valve with embolic filter: Experiments and simulations, in: Proceedings of VII Congress of the National Group of Bioengineering.

Carbonaro, D., Gallo, D., Morbiducci, U., Audenino, A., Chiastra, C., 2021. In silico biomechanical

Post-print

design of the metal frame of transcatheter aortic valves: multi-objective shape and cross-sectional size optimization. Struct. Multidiscip. Optim. 64, 1825–1842. https://doi.org/10.1007/s00158-021-02944-w

Corti, A., Chiastra, C., Colombo, M., Garbey, M., Migliavacca, F., Casarin, S., 2020. A fully coupled computational fluid dynamics – agent-based model of atherosclerotic plaque development: Multiscale modeling framework and parameter sensitivity analysis. Comput. Biol. Med. 118, 103623. https://doi.org/10.1016/j.compbiomed.2020.103623

Corti, A., Colombo, M., Rozowsky, J.M., Casarin, S., He, Y., Carbonaro, D., Migliavacca, F., Rodriguez Matas, J.F., Berceli, S.A., Chiastra, C., 2022. A predictive multiscale model of in-stent restenosis in femoral arteries: linking haemodynamics and gene expression with an agent-based model of cellular dynamics. J. R. Soc. Interface 19, 20210871. https://doi.org/https://doi.org/10.1098/rsif.2021.0871

Cubero-Gallego, H., Dam, C., Meca, J., Avanzas, P., 2020. Transcatheter aortic valve replacement (TAVR): expanding indications to low-risk patients. Ann. Transl. Med. 8, 960–960. https://doi.org/10.21037/atm.2020.03.155

Dasi, L.P., Hatoum, H., Kheradvar, A., Zareian, R., Alavi, S.H., Sun, W., Martin, C., Pham, T., Wang, Q., Midha, P.A., Raghav, V., Yoganathan, A.P., 2017. On the mechanics of transcatheter aortic valve replacement. Ann. Biomed. Eng. 45, 310–331. https://doi.org/10.1007/s10439-016-1759-3

De Jaegere, P., De Santis, G., Rodriguez-Olivares, R., Bosmans, J., Bruining, N., Dezutter, T., Rahhab, Z., El Faquir, N., Collas, V., Bosmans, B., Verhegghe, B., Ren, C., Geleinse, M., Schultz, C., Van Mieghem, N., De Beule, M., Mortier, P., 2016. Patient-specific computer modeling to predict aortic regurgitation after transcatheter aortic valve replacement. JACC Cardiovasc. Interv. 14, 508–512. https://doi.org/10.1016/j.jcin.2016.01.003

Deb, K., Pratap, A., Agarwal, S., Meyarivan, T., 2002. A fast and elitist multiobjective genetic

Post-print

algorithm: NSGA-II. IEEE Trans. Evol. Comput. 6, 182–197. https://doi.org/10.1109/4235.996017

Duerig, T.W., Tolomeo, D.E., Wholey, M., 2000. An overview of superelastic stent design. Minim. Invasive Ther. Allied Technol. 9, 235–46. https://doi.org/10.1080/13645700009169654

Fanning, J.P., Platts, D.G., Walters, D.L., Fraser, J.F., 2013. Transcatheter aortic valve implantation (TAVI): Valve design and evolution. Int. J. Cardiol. 168, 1822–1831. https://doi.org/10.1016/j.ijcard.2013.07.117

FDA, 2020. Technical considerations for non- clinical assessment of medical devices containing Nitinol - Guidance for industry and food and drug administration staff.

Finotello, A., Gorla, R., Brambilla, N., Bedogni, F., Auricchio, F., Morganti, S., 2021. Finite element analysis of transcatheter aortic valve implantation: Insights on the modelling of self-expandable devices. J. Mech. Behav. Biomed. Mater. 123, 104772. https://doi.org/10.1016/j.jmbbm.2021.104772

Finotello, A., Morganti, S., Auricchio, F., 2017. Finite element analysis of TAVI: Impact of native aortic root computational modeling strategies on simulation outcomes. Med. Eng. Phys. 47, 2–12. https://doi.org/10.1016/j.medengphy.2017.06.045

Ghosh, R.P., Marom, G., Bianchi, M., D'souza, K., Zietak, W., Bluestein, D., 2020. Numerical evaluation of transcatheter aortic valve performance during heart beating and its post-deployment fluid–structure interaction analysis. Biomech. Model. Mechanobiol. 19, 1725–1740. https://doi.org/10.1007/s10237-020-01304-9

Gunning, P.S., Vaughan, T.J., McNamara, L.M., 2014. Simulation of self expanding transcatheter aortic valve in a realistic aortic root: Implications of deployment geometry on leaflet deformation. Ann. Biomed. Eng. 42, 1989–2001. https://doi.org/10.1007/s10439-014-1051-3

Henderson, E., Nash, D.H., Dempster, W.M., 2011. On the experimental testing of fine Nitinol wires

Post-print

for medical devices. J. Mech. Behav. Biomed. Mater. 4, 261–268. https://doi.org/10.1016/j.jmbbm.2010.10.004

Hickernell, F.J., Hong, H.S., L'écuyer, P., Lemieux, C., 2001. Extensible lattice sequences for quasi-Monte Carlo quadrature. SIAM J. Sci. Comput. 22, 1117–1138. https://doi.org/10.1137/S1064827599356638

Hodgson, D., Russell, S., 2000. Nitinol melting, manufacture and fabrication. Minim. Invasive Ther. Allied Technol. 9, 61–65. https://doi.org/10.3109/13645700009063051

Howard, C., Jullian, L., Joshi, M., Noshirwani, A., Bashir, M., Harky, A., 2019. TAVI and the future of aortic valve replacement. J. Card. Surg. 34, 1577–1590. https://doi.org/10.1111/jocs.14226

ISO, 2013. Cardiovascular omplants - Cardiac valve prostheses - Part 3: Heart valve substitutes implanted by transcatheter techniques. ISO 5840-3.

Jones, B.M., Krishnaswamy, A., Tuzcu, E.M., Mick, S., Jaber, W.A., Svensson, L.G., Kapadia, S.R., 2017. Matching patients with the ever-expanding range of TAVI devices. Nat. Rev. Cardiol. 14, 615–626. https://doi.org/10.1038/nrcardio.2017.82

Jones, D.R., Schonlau, M., Welch, W.J., 1998. Efficient global optimization of expensive black-box functions. J. Glob. Optim. 13, 455–492. https://doi.org/10.1023/A:1008306431147

Kumar, S., Moseman, B., Vietmeier, K., 2014. Stent geometry and radial force comparison of Portico vs CoreValve. Circulation 130. https://doi.org/10.1111/j.1095-8312.1978.tb00013.x

Kusneri, J., Luraghi, G., Khodaeei, F., Matas, J.F.L.R., Migliavacca, F., Edelman, E.R., Nezami, F.R., 2021. Understanding TAVR device expansion as it relates to morphology of the bicuspid aortic valve: A simulation study. PLoS One 16, 1–9. https://doi.org/10.1371/journal.pone.0251579

Lagoudas, D., Hartl, D., Chemisky, Y., MacHado, L., Popov, P., 2012. Constitutive model for the numerical analysis of phase transformation in polycrystalline shape memory alloys. Int. J. Plast. 32–33, 155–183. https://doi.org/10.1016/j.ijplas.2011.10.009

Post-print

Liu, H.S., Mishnaevsky, L., 2013. Martensitic transformations in nanostructured nitinol: Finite element modeling of grain size and distribution effects. Comput. Mater. Sci. 76, 27–36. https://doi.org/10.1016/j.commatsci.2012.11.032

Luraghi, G., Matas, J.F.R., Beretta, M., Chiozzi, N., Iannetti, L., Migliavacca, F., 2020. The impact of calcification patterns in transcatheter aortic valve performance: A fluid-structure interaction analysis. Comput. Methods Biomech. Biomed. Engin. 24, 375–383. https://doi.org/10.1080/10255842.2020.1817409

Mack, M.J., Leon, M.B., Thourani, V.H., Makkar, R., Kodali, S.K., Russo, M., Kapadia, S.R., Malaisrie, S.C., Cohen, D.J., Pibarot, P., Leipsic, J., Hahn, R.T., Blanke, P., Williams, M.R., McCabe, J.M., Brown, D.L., Babaliaros, V., Goldman, S., Szeto, W.Y., Genereux, P., Pershad, A., Pocock, S.J., Alu, M.C., Webb, J.G., Smith, C.R., 2019. Transcatheter aortic-valve replacement with a balloon-expandable valve in low-risk patients. N. Engl. J. Med. 385, 2477–2484. https://doi.org/10.1056/nejmoa1814052

Mao, W., Wang, Q., Kodali, S., Sun, W., 2018. Numerical parametric study of paravalvular leak following a transcatheter aortic valve deployment into a patient-specific aortic root. J. Biomech. Eng. 140, 1–11. https://doi.org/10.1115/1.4040457

Marino, S., Hogue, I.B., Ray, C.J., Kirschner, D.E., 2008. A methodology for performing global uncertainty and sensitivity analysis in systems biology. J. Theor. Biol. 254, 178–196. https://doi.org/10.1016/j.jtbi.2008.04.011

Marquis-Gravel, G., Redfors, B., Leon, M.B., Généreux, P., 2016. Medical treatment of aortic stenosis. Circulation 134, 1766–1784. https://doi.org/10.1161/CIRCULATIONAHA.116.023997

McGee, O.M., Gunning, P.S., McNamara, A., McNamara, L.M., 2019a. The impact of implantation depth of the Lotus^{TM} valve on mechanical stress in close proximity to the bundle of His. Biomech. Model. Mechanobiol. 18, 79–88. https://doi.org/10.1007/s10237-018-1069-9

Post-print

McGee, O.M., Sun, W., McNamara, L.M., 2019b. An in vitro model quantifying the effect of calcification on the tissue–stent interaction in a stenosed aortic root. J. Biomech. 82, 109–115. https://doi.org/10.1016/j.jbiomech.2018.10.010

Morganti, S., Brambilla, N., Petronio, A.S., Reali, A., Bedogni, F., Auricchio, F., 2016. Prediction of patient-specific post-operative outcomes of TAVI procedure: The impact of the positioning strategy on valve performance. J. Biomech. 49, 2513–2519. https://doi.org/10.1016/j.jbiomech.2015.10.048

Morganti, S., Conti, M., Aiello, M., Valentini, A., Mazzola, A., Reali, A., Auricchio, F., 2014. Simulation of transcatheter aortic valve implantation through patient-specific finite element analysis: Two clinical cases. J. Biomech. 47, 2547–2555. https://doi.org/10.1016/j.jbiomech.2014.06.007

Mummert, J., Sirois, E., Sun, W., 2013. Quantification of biomechanical interaction of transcatheter aortic valve stent deployed in porcine and ovine hearts. Ann. Biomed. Eng. 41, 577–586. https://doi.org/10.1007/s10439-012-0694-1

Mwangi, J.W., Nguyen, L.T., Bui, V.D., Berger, T., Zeidler, H., Schubert, A., 2019. Nitinol manufacturing and micromachining: A review of processes and their suitability in processing medical-grade nitinol. J. Manuf. Process. 38, 355–369. https://doi.org/10.1016/j.jmapro.2019.01.003

Nappi, F., Mazzocchi, L., Timofeva, I., MacRon, L., Morganti, S., Singh, S.S.A., Attias, D., Congedo, A., Auricchio, F., 2020. A finite element analysis study from 3D CT to predict transcatheter heart valve thrombosis. Diagnostics 10. https://doi.org/10.3390/diagnostics10040183

Nemat-Nasser, S., Guo, W.G., 2006. Superelastic and cyclic response of NiTi SMA at various strain rates and temperatures. Mech. Mater. 38, 463–474. https://doi.org/10.1016/j.mechmat.2005.07.004

Otsuka, K., Ren, X., 2005. Physical metallurgy of Ti-Ni-based shape memory alloys. Prog. Mater. Sci.

Post-print

50, 511–678. https://doi.org/10.1016/j.pmatsci.2004.10.001

Ovcharenko, E.A., Klyshnikov, K.U., Yuzhalin, A.E., Savrasov, G. V., Kokov, A.N., Batranin, A. V., Ganyukov, V.I., Kudryavtseva, Y.A., 2016. Modeling of transcatheter aortic valve replacement: Patient specific vs general approaches based on finite element analysis. Comput. Biol. Med. 69, 29–36. https://doi.org/10.1016/j.compbiomed.2015.12.001

Pant, S., Bressloff, N.W., Limbert, G., 2012. Geometry parameterization and multidisciplinary constrained optimization of coronary stents. Biomech. Model. Mechanobiol. 11, 61–82. https://doi.org/10.1007/s10237-011-0293-3

Pasta, S., Gandolfo, C., 2021. Computational analysis of self-expanding and balloon-expandable transcatheter heart valves. Biomechanics 1, 43–52. https://doi.org/10.3390/biomechanics1010004

Pawade, T., Clavel, M.A., Tribouilloy, C., Dreyfus, J., Mathieu, T., Tastet, L., Renard, C., Gun, M., Jenkins, W.S.A., MacRon, L., Sechrist, J.W., Lacomis, J.M., Nguyen, V., Gay, L.G., Calabria, H.C., Ntalas, I., Cartlidge, T.R.G., Prendergast, B., Rajani, R., Evangelista, A., Cavalcante, J.L., Newby, D.E., Pibarot, P., Zeitoun, D.M., Dweck, M.R., 2018. Computed tomography aortic valve calcium scoring in patients with aortic stenosis. Circ. Cardiovasc. Imaging 11, 1–11. https://doi.org/10.1161/CIRCIMAGING.117.007146

Petrini, L., Bertini, A., Berti, F., Pennati, G., Migliavacca, F., 2017a. The role of inelastic deformations in the mechanical response of endovascular shape memory alloy devices. Proc. Inst. Mech. Eng. Part H J. Eng. Med. 231, 391–404. https://doi.org/10.1177/0954411917696336

Petrini, L., Dordoni, E., Allegretti, D., Pott, D., Kütting, M., Migliavacca, F., Pennati, G., 2017b. Simplified multistage computational approach to assess the fatigue behavior of a niti transcatheter aortic valve during in vitro tests: A proof-of-concept study. J. Med. Devices, Trans. ASME 11, 1–11. https://doi.org/10.1115/1.4035791

Popma, J.J., Deeb, G.M., Yakubov, S.J., Mumtaz, M., Gada, H., O'Hair, D., Bajwa, T., Heiser, J.C.,

Post-print

Merhi, W., Kleiman, N.S., Askew, J., Sorajja, P., Rovin, J., Chetcuti, S.J., Adams, D.H., Teirstein, P.S., Zorn, G.L., Forrest, J.K., Tchétché, D., Resar, J., Walton, A., Piazza, N., Ramlawi, B., Robinson, N., Petrossian, G., Gleason, T.G., Oh, J.K., Boulware, M.J., Qiao, H., Mugglin, A.S., Reardon, M.J., 2019. Transcatheter aortic-valve replacement with a self-expanding valve in low-risk patients. N. Engl. J. Med. 380, 1706–1715. https://doi.org/10.1056/nejmoa1816885

Rasmussen, C.E., Williams, C.K.I., 2018. Gaussian processes for machine learning, MIT Press, Massachusetts.

Rocatello, G., De Santis, G., De Bock, S., De Beule, M., Segers, P., Mortier, P., 2019a. Optimization of a transcatheter heart valve frame using patient-specific computer simulation. Cardiovasc. Eng. Technol. 10, 456–468. https://doi.org/10.1007/s13239-019-00420-7

Rocatello, G., El Faquir, N., de Backer, O., Swaans, M.J., Latib, A., Vicentini, L., Segers, P., De Beule, M., de Jaegere, P., Mortier, P., 2019b. The impact of size and position of a mechanical expandable transcatheter aortic valve: novel insights through computational modelling and simulation. J. Cardiovasc. Transl. Res. 12, 435–446. https://doi.org/10.1007/s12265-019-09877-2

Rotman, O.M., Bianchi, M., Ghosh, R.P., Kovarovic, B., Bluestein, D., 2018. Principles of TAVR valve design, modelling, and testing. Expert Rev. Med. Devices 15, 771–791. https://doi.org/10.1080/17434440.2018.1536427

Stoeckel, D., Pelton, A., Duerig, T., 2004. Self-expanding Nitinol stents: Material and design considerations. Eur. Radiol. 14, 292–301. https://doi.org/10.1007/s00330-003-2022-5

Sturla, F., Ronzoni, M., Vitali, M., Dimasi, A., Vismara, R., Preston-Maher, G., Burriesci, G., Votta, E., Redaelli, A., 2016. Impact of different aortic valve calcification patterns on the outcome of transcatheter aortic valve implantation: A finite element study. J. Biomech. 49, 2520–2530. https://doi.org/10.1016/j.jbiomech.2016.03.036

Tabata, N., Sinning, J.M., Kaikita, K., Tsujita, K., Nickenig, G., Werner, N., 2019. Current status and

Post-print

future perspective of structural heart disease intervention. J. Cardiol. 74, 1–12. https://doi.org/10.1016/j.jjcc.2019.02.022

Thubrikar, M.J., Aouad, J., Nolan, S.P., 1986. Patterns of calcific deposits in operatively excised stenotic or purely regurgitant aortic valves and their relation to mechanical stress. Am. J. Cardiol. 58, 304–308. https://doi.org/10.1016/0002-9149(86)90067-6

Tiyerili, V., Sötemann, D., Grothusen, C., Eckel, C., Becher, M.U., Blumenstein, J., Nef, H., Helge Möllmann, 2022. Latest advances in transcatheter aortic valve implantation (2022). Surg. Technol. Int. 40, 1478. https://doi.org/10.52198/21.STI.40.CV1478

Tzamtzis, S., Viquerat, J., Yap, J., Mullen, M.J., Burriesci, G., 2013. Numerical analysis of the radial force produced by the Medtronic-CoreValve and Edwards-SAPIEN after transcatheter aortic valve implantation (TAVI). Med. Eng. Phys. 35, 125–130. https://doi.org/10.1016/j.medengphy.2012.04.009

Valiev, R.Z., Prokofiev, E.A., Kazarinov, N.A., Raab, G.I., Minasov, T.B., Stráský, J., 2020. Developing nanostructured Ti alloys for innovative implantable medical devices. Materials (Basel). 13, 967. https://doi.org/10.3390/ma13040967

Wang, Q., Kodali, S., Primiano, C., Sun, W., 2015. Simulations of transcatheter aortic valve implantation: implications for aortic root rupture. Biomech. Model. Mechanobiol. 14, 29–38. https://doi.org/10.1007/s10237-014-0583-7

Wang, Q., Sirois, E., Sun, W., 2012. Patient-specific modeling of biomechanical interaction in transcatheter aortic valve deployment. J. Biomech. 45, 1965–1971. https://doi.org/10.1016/j.jbiomech.2012.05.008

Wiegerinck, E.M.A., Van Kesteren, F., Van Mourik, M.S., Vis, M.M., Baan, J., 2016. An up-to-date overview of the most recent transcatheter implantable aortic valve prostheses. Expert Rev. Med. Devices 13, 31–45. https://doi.org/10.1586/17434440.2016.1120665

Post-print

Accepted manuscript at https://linkinghub.elsevier.com/retrieve/pii/S1751-6161(22)00528-8

Post-print